ABSTRACT

SINGLE-AXIS AGONISTIC MOTION CONTROL SYSTEM WITH ELECTRO-MAGNETIC ACTUATORS

by
Alexander Rokhvarg

A novel single-axis motion control system using solenoid electromagnet actuators is built and successfully controlled using a non-linear real-time control algorithm. Procedures for defining and modeling the electromagnetic actuator are established and implemented. Discrete-time nonlinear control law with global asymptotic stability and zero steady-state error is designed and numerically optimized. Stable operation with small-signal 0dB crossover frequency of 370 Rad/sec and positioning RMS steady-state error of better than 4 micron is achieved. Time domain parameters are verified on a working prototype. A step reference response positioning a 0.35 Kg mass payload over 1 cm travel in under 30 milliseconds is demonstrated.

SINGLE-AXIS AGONISTIC MOTION CONTROL SYSTEM WITH ELECTRO-MAGNETIC ACTUATORS

by
Alexander Rokhvarg

A Thesis
Submitted to the Faculty of
New Jersey Institute of Technology
in Partial Fulfillment of the Requirements for the Degree of
Master of Science in Electrical Engineering

Department of Electrical and Computer Engineering

January 1995

APPROVAL SHEET

SINGLE-AXIS AGONISTIC MOTION CONTROL SYSTEM WITH ELECTRO-MAGNETIC ACTUATORS

Alexander Rokhvarg

Dr. Bernard Friedland, Thesis Advisor — Date
Distinguished Professor,
ECE Department

Dr. Andrew U. Meyer — Date
Professor, Coordinator, Control Systems
ECE Department

Dr. Timothy N. Chang — Date
Assistant Professor
ECE Department

Dr. Walid Hubbi — Date
Associate Professor
ECE Department

BIOGRAPHICAL SKETCH

Author: Alexander Rokhvarg

Degree: Master of Science in Electrical Engineering

Date: January 1995

Undergraduate and Graduate Education

- Master of Science in Electrical Engineering,
  New Jersey Institute of Technology,
  Newark, New Jersey, 1995

- Bachelor of Science in Electrical Engineering,
  New York Institute of Technology,
  Old Westbury, New York, 1990

Major: Electrical Engineering

Accreditation

- Licensed Professional Engineer, 1992

This thesis is dedicated to my wife Marina and son Lawrence.
Their supreme patience and understanding made it all possible.

ACKNOWLEDGMENT

The author wishes to express gratitude to Professor Bernard Friedland, whose appreciation for control theory was contagious. And for his encouragement, inspiration and guidance as thesis advisor I shall remain thankful.

Sincere appreciation to Dr. Timothy Chang for his valuable assistance and insights in the field of real-time control and numerical optimization applications.

A special word of thanks to my employer, Mr. Richard F. Blake, founder and CEO of Transistor Devices Inc. His encouragement and continuing support of higher education helped make this work possible.

TABLE OF CONTENTS

TABLE OF CONTENTS

(Continued)

TABLE OF CONTENTS

(Continued)

LIST OF TABLES

LIST OF FIGURES

Figure **Page**

LIST OF FIGURES

(Continued)

Figure **Page**

LIST OF FIGURES

(Continued)

Figure **Page**

LIST OF UNITS

All measurements and calculations in this document are consistent with the International System of Units, abbreviated SI. The following is the list of most frequently used units and measures.

Quantity	**Name of Unit**	**Symbol**
	SI Base Units	
length	meter	m
mass	Kilogram	Kg
time	second	s
electric current	Ampere	A
	SI Derived Units	
frequency	Hertz	Hz 1/s
speed	meter per second	m/s
acceleration	meter per second squared	m/s^2
force	Newton	N $Kg \cdot m/s^2$
energy	Joules	J N·m
power	watt	W J/s

CHAPTER 1

INTRODUCTION

The term *agonistic* control refers to a novel method of motion control (pioneered by an NJIT research team) where the workpiece is manipulated by multiple tendons that remain under tension while pulling it to the desired location.

This versatile control strategy offers numerous advantages over the conventional drive systems. High bandwidth, negligible friction and backlash, high precision, and low cost are some features that render the agonistic control technology potentially superior for the use in the area of agile manufacturing.

Another advantage of agonistic control is a wide choice of actuators. The flexible tendons in the agonistic control plant may be energized by d-c motors, voice coils, or electromagnets just to name a few.

Ongoing research at NJIT focused on agonistic control using d-c motors as actuators has yielded very encouraging results. A single-axis and a two-axis model are under development. Control algorithms for multiple degree of freedom systems are also under investigation.

This thesis concentrates on the development of a single-axis agonistic control system actuated via two solenoid electromagnets. The choice of solenoid as an actuator was based on its low cost and high energy density. Another advantage offered by solenoid actuators in agonistic configuration is virtual non-existence of friction. The force lines generated by the current in the coil tend to center the magnetic plunger inside the coil cavity.

Electromagnets are dynamically unstable and highly nonlinear. Nevertheless, electromagnetic control is quite feasible as attested by numerous magnetic levitation examples.

In most levitation systems, the closed-loop bandwidth and positioning accuracy become tradeoffs for system robustness. The demands of agile manufacturing tools are much more rigorous than simple global asymptotic stability. To contribute to agile manufacturing procedures, tools or processes, the control laws in agonistic systems must maximize speed of response as well as provide zero steady-state error.

This research concentrates on the development of a single-axis agonistic motion control system actuated by two solenoid electromagnets. The investigation process and topics include:

- Examination of the single-axis agonistic plant,
- Modeling of the solenoid electromagnet actuator, developing the static defining equation, and measuring high frequency dynamic characteristics,
- Design and simulation of a suitable control law that assures global asymptotic stability and zero steady-state error,
- Selection of optimal performance parameters based on practical design considerations,
- Translation of real-time control law into computer code,
- Construction and test of a working prototype, and
- Closed loop performance verification.

While the focus of this thesis is the feasibility study of single axis electromagnetically actuated agonistic motion control, the broader application of general theory and

procedures described herein may have many practical applications. High speed precision articulation is an essential element in many advanced processes. For example, Computer Integrated Manufacturing processes such as in semiconductor fabrication require precise high speed motion control for pick and place die attachers and wire bonders.

That cost and complexity can be reduced in such applications and environments warrants further investigation and evolutionary expansion into development of multi-axis agonistic motion control systems.

1.1 Single-Axis Agonistic System Construction

The essential features of the single-axis agonistic motion control system are depicted in figure 1.1.

In the heart of the motion control system is the agonistic control plant. The plant consist of a *payload* whose position is governed by the net force exerted by the two *solenoid electromagnets*.

The payload position feedback is measured by a linear transducer comprising a *linear potentiometer* whose plunger is fastened to the payload, a precision *voltage reference* and a *scaling amplifier* .

The output of the position transducer is followed with an anti-aliasing *Low-Pass Filter* in order to limit the exposure of the Analog - to- Digital converters to frequencies higher than the Nyquist rate .

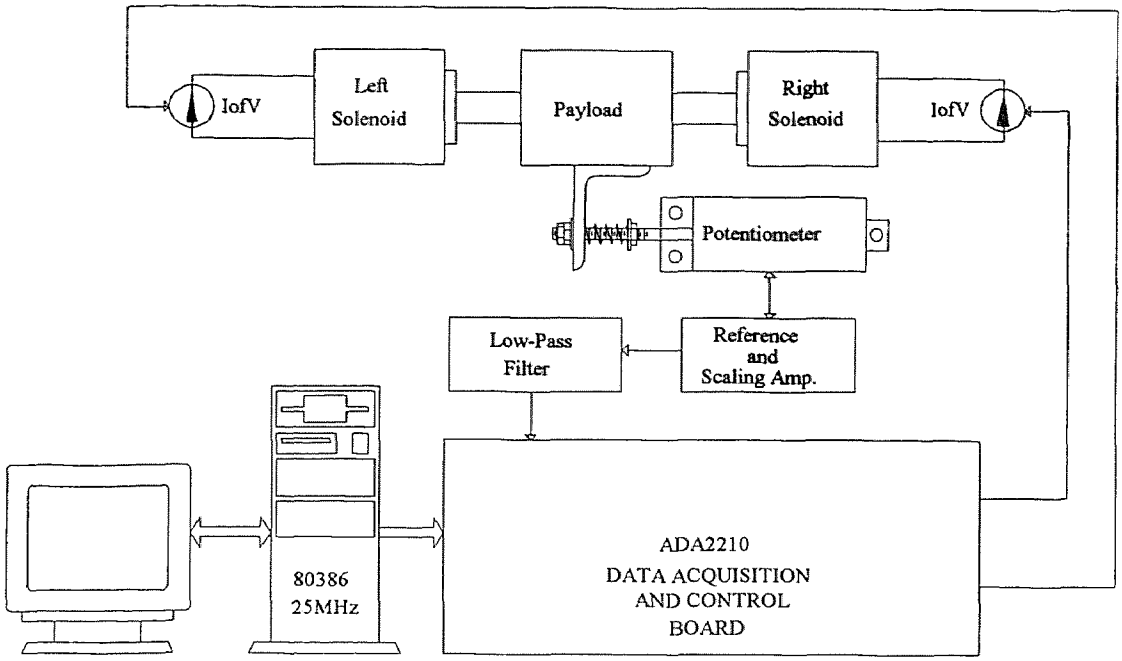

Figure 1.1 Single-Axis Agonistic Motion Control System

The control algorithm for the single-axis agonistic control is implemented digitally on an IBM compatible 80386 25 MHz computer equipped with ADA2210 *Advanced Data Acquisition and Control board.*

The outputs generated by the control board are used to program the *Voltage Controlled Current Sources* (I of V) that energize the solenoids.

A detailed systems hardware description is presented in Chapter 6 and Appendix A of this document.

1.2 Plant Definition

A simplified block diagram of the single-axis agonistic plant is shown in Figure 1.2.

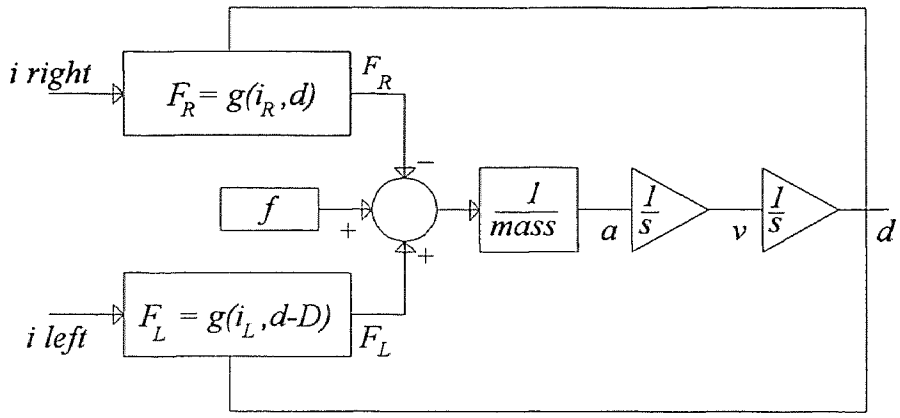

Figure 1.2 Simplified block diagram of the single-axis agonistic plant.

This is a nonlinear second order dynamic system that obeys the following relation

$$\ddot{d} = \frac{1}{m}(F_L - F_R + f) \tag{1.1}$$

where $F_R = g(i_R, d_R)$ and $F_L = g(i_L, d_L)$ are the forces exerted by the left and right solenoids respectively and f is the exogenous disturbance force designed to represent friction (mostly due to potentiometer actuation force) and other unmodeled parameters.

The function $g(i, d)$ is the nonlinear algebraic dependency that describes the force developed by the solenoid at a given plunger displacement and coil excitation current. This dependency is examined in more detail later in this document.

The right and left plunger displacements (d_R and d_L) are not independent but rather interrelated through the total travel distance (D) such that $D = d_R + d_L$.

The output variables in agonistic plant are the *payload position*, d, and the *tension* in the tendons.

The tension in each tendon is the force produced by its respective solenoid. It must be emphasized that the *minimum* tension is to be controlled. As seen from figure 1.3, the forces F_R and F_L act on the payload in opposing directions, thus it is the net force (F_L - F_R) that causes payload to move. With zero acceleration the net force is zero and the tension in each tendon is the same. However, under dynamic conditions a net force must be generated to produce a change in the payload position, therefore higher tension in the tendon of the device that is doing the work is developed.

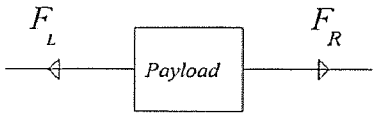

Figure 1.3 Force Distribution in Single-Axis System

CHAPTER 2

ACTUATOR PARAMETER IDENTIFICATION

The actuator chosen in this project is a solenoid electromagnet whose output is the force and input is the coil excitation current. It is a well known fact that the solenoid characteristics are nonlinear. Nonlinearity stems from three major factors. First is the ideal solenoid's polynomial relation of the force, excitation current and solenoid plunger position, second factor is the nonuniform field distribution effects, and third factor is the ferromagnetic media nonlinearity.

While basic dependencies for the ideal solenoid may be readily established, the nonuniform field distribution and ferromagnetic media nonlinearities make it virtually impossible to obtain an accurate mathematical representation of the practical solenoid electromagnet by analysis. However knowing the basic dependencies, empirical data may be collected and then "fitted" with an acceptable mathematical description.

The following section will concentrate on identification of solenoid magnet parameters, basic background theory, measurement techniques and equipment, and measured result interpretation. The ideal solenoid electromagnet characteristics are examined in paragraph 2.1 and factors contributing to deviation from the ideal model are discussed. The empirical data are collected in paragraph 2.2. and used in paragraph 2.3 for establishing a static time-invariant memoryless algebraic dependency known as the *defining equation.*

2.1 Background Theory

2.1.1 Ideal Solenoid Characteristics

The basic dependency for the force produced by the electromagnet may be derived with the help of the energy method of forces [7] where knowing the total stored energy in the magnetic field as a function of flux and position, at any fixed value of flux, the force is found from

$$f_x = -\left.\frac{dW}{dx}\right|_{\Phi} \tag{2.1}$$

If the core and the slug material are assumed to be infinitely permeable the force on the moveable slug in the magnetic circuit shown in figure 2.1 is given by

$$f_x = \frac{1}{2} I^2 \frac{dL(x)}{dx} = -\frac{\mu_o N^2 A I^2}{2x^2} \tag{2.2}$$

The minus sign means that the force is opposite to the direction of increasing x, so that the moveable piece is attracted to the coil.

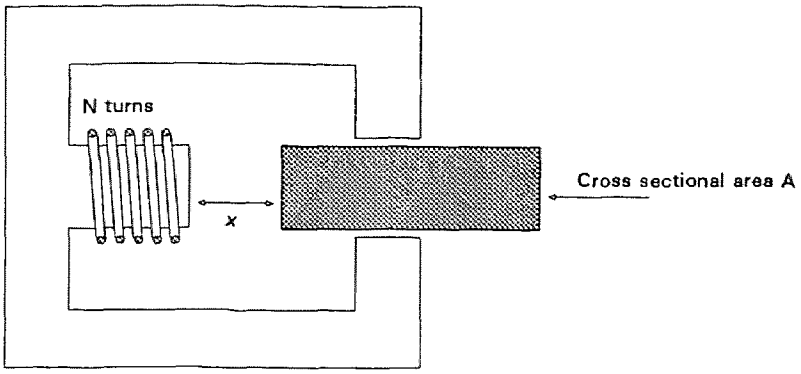

Figure 2.1 Magnetic circuit for Ideal solenoid

2.1.2 Non-linear Effects Due to Non-uniform Field Distribution

In order to make derivation in section 2.1.1 feasible, the solenoid field distribution was assumed to be uniform. In practice this is not the case. Even in the case of uniform magnetic media, the finite permeability of the core and slug can no longer confine the **H**-field to the air gap, thus the field weakens and the actual force is lower then predicted by equation 2.2.

Furthermore, finite permeability gives rise to the leakage flux where not all flux lines are confined to the ferromagnetic media. The leakage flux effects are more pronounced as the plunger displacement increases. The fringing flux changes the field's incident angles thus further reducing the actual force produced by the electromagnet.

Another source of nonuniform field distribution is the varying cross-sectional area of the plunger. In addition to uniform rod shaped slugs, most manufacturers produce solenoids with tapered plungers. The tapered plunger construction renders a smother force-distance characteristics. The solenoid used in the prototype had a 60° taper angle.

2.1.3 Nonlinear Effects Contributed by Ferromagnetic Materials

Virtually all electromagnets are constructed with ferromagnetic materials. These materials exhibit a complex dependency between the flux (Φ) and the coil current(I). In addition to permeability variation that depends on the magnitude of applied magnetizing force, the ferromagnetic materials exhibit a memory element known as hysteresis.

The flux in the electromagnetic circuit is directly related to the force produced by the electromagnet, thus examining the dependency of the flux on excitation current in ferromagnetic media will be helpful in predicting the behavior of the solenoid electromagnet.

It is customary to represent the magnetization characteristics in terms of magnetizing forces H, and flux density B where B and H for uniform magnetic fields defined as

$$B = k_1 \Phi \qquad \text{and} \qquad H = k_2 i$$

The constants k_1 and k_2 depend on the electromagnets geometry and the system of units. The magnetizing force H, and flux density B are vectors, however, this discussion is limited to one particular geometry where the field direction is known, thus only the magnitudes of the fields are of interest.

A typical unidirectional ferromagnetic magnetization curve is shown in figure 2.2 [6].

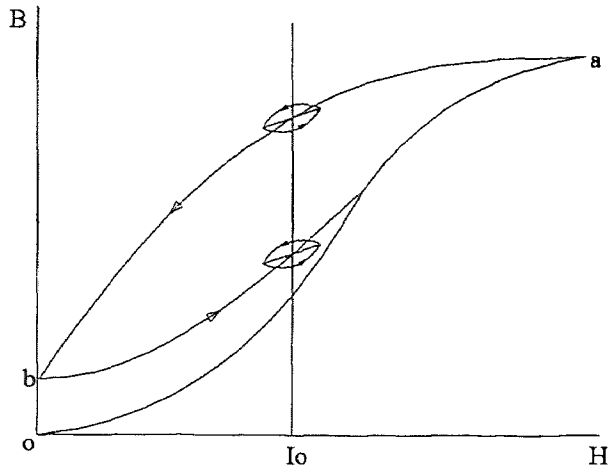

Figure 2.2 Typical Unidirectional Ferromagnetic Magnetization Curve

If the magnetizing field is varied from zero in a positive direction, the flux density in the specimen will follow the initial magnetization curve as shown by the segment *oa* in figure 2.2.

As the magnetizing force is now decreased to zero, it is noted that the flux density follows the curve *ab*. The B-H curve for the decreasing values of magnetizing force does not correspond with the original rising curve. There is a flux density *ob* remaining in the material after the magnetizing force has been returned to zero. It is called the residual flux density, and is determined by the *retentivity* of the material. Consequent increase of the magnetizing force will cause the flux density to follow the curve *ba* thus closing the hysteresis loop. The hysteresis effect is present in ferromagnetic even under virtually static conditions. Increase in excitation frequency will widen the hysteresis loop.

It is clear from figure 2.2 that the same current I_0 will produce two distinct values of flux density B_1, and B_2 dependent on the history of the current excursion and thus distinct values of force.

A small perturbation around an operating point will produce its own hysteresis loop. This phenomenon will have a noticeable effect on actuator dynamic characteristics in the form of lower effective gain and additional phase lag. Given a constant excitation signal, the area encircled by the minor hysteresis loop and thus the associated phase shift and small signal gain reduction will increase with frequency.

Biasing a magnetic material with constant H-field will shift the minor loop but will not have a noticeable effect on its shape. Therefore, the phase shift and small signal gain reduction associated with the minor hysteresis will vary with frequency and plunger displacement and not with DC operating current.

2.2 Measurement Results and Procedures

2.2.1 Measurement Setup

To obtain the data used in this document, a thin beam load cell setup shown in figure 2.3 was used. The thin beam load cell is an integrated strain gauge that includes balancing, compensating and conductive elements and is laminated to the beam to provide refined linearity and temperature stability.

The force applied to a beam causes a small deflection (strain). The deflection is registered by four strain gauge elements. The strain gauge elements are connected in a Wheatstone Bridge configuration such that the bridge output voltage is proportional to the applied force.

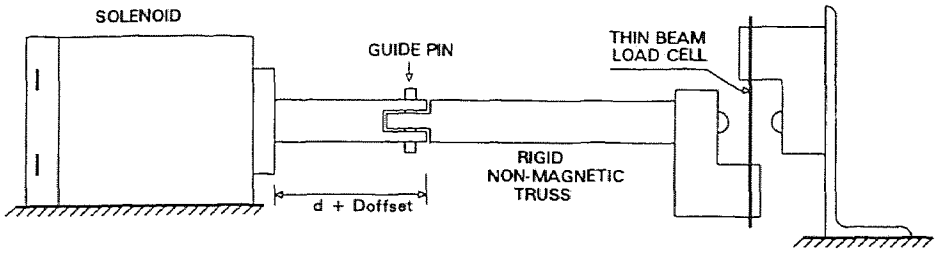

Figure 2.3 Measurement Setup Using Thin Beam Load Cell

2.2.2 Static Characteristics Measurements

Data collection procedure was automated with the help of the 2210 Advanced Industrial Control board manufactured by Real Time Devices, Inc. , the same board that is used in real-time control implementation.

The board was programmed to read and store the force output at 0.1 seconds intervals while sweeping the solenoid current from 0A to 3A and back to 0A for a total of 5 cycles.

Data were collected for nine distinct plunger displacement settings. The results obtained for displacement settings 0.2", 0.4", 0.6" (0.00508 m, 0.0101m, 0.01524m respectively) are shown in figures 2.4 through 2.6. As expected, in all three cases, the force produced by initially demagnetized plunger starts at zero and follows the initial magnetization curve. As current is reduced to zero, there is a small residual force remaining. Further increase of current increases the force from the residual point until it

converges with the initial magnetization curve. The remaining magnetizing cycles almost ideally follow the trajectory of the last cycle.

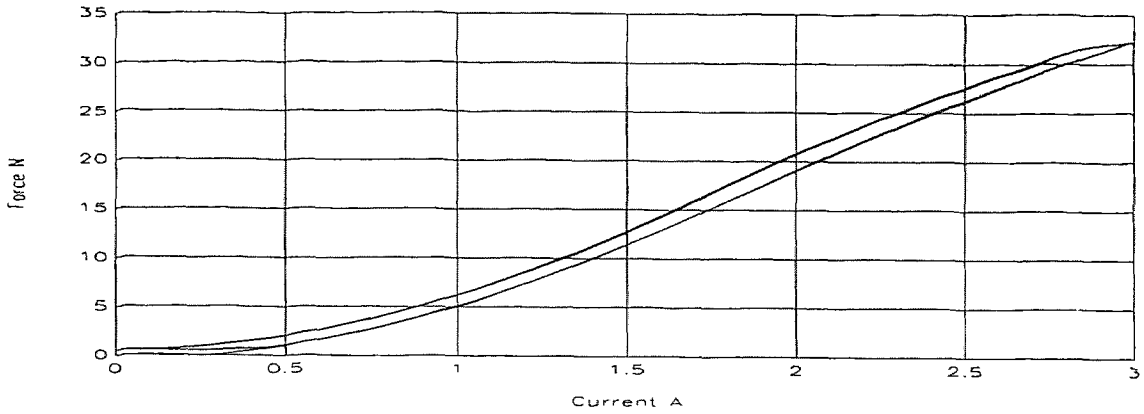

Figure 2.4 Low Frequency Hysteresis with Plunger Displacement 0.2" (0.00508m)

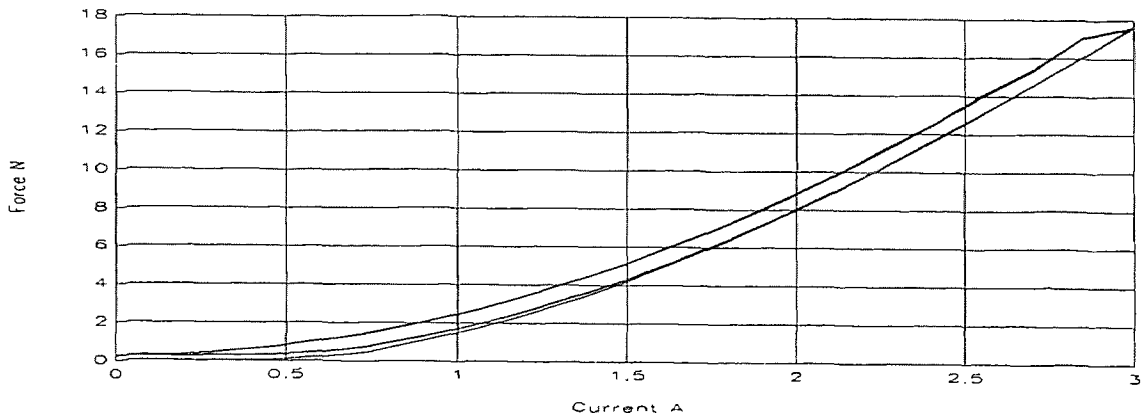

Figure 2.5 Low Frequency Hysteresis with Plunger Displacement 0.4" (0.0101 m)

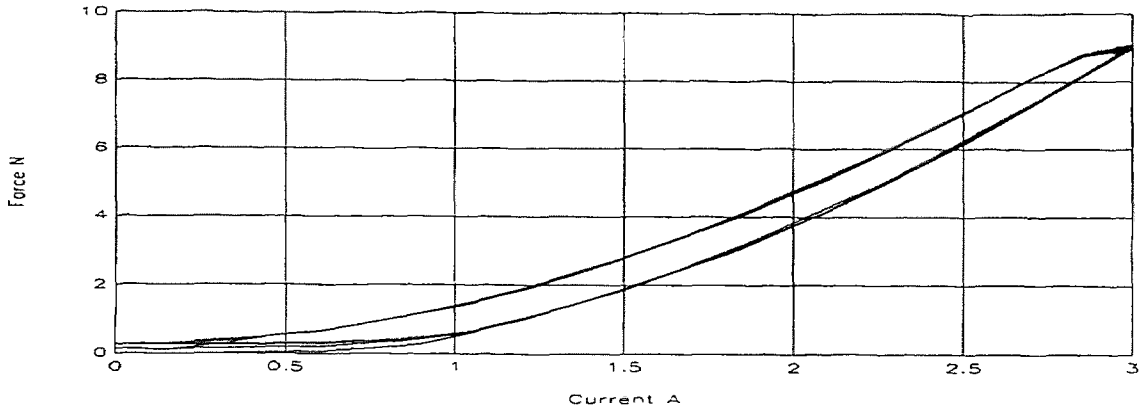

Figure 2.6 Low Frequency Hysteresis with Plunger Displacement 0.6" (0.01524m)

It may be observed that each static hysteresis scan starts in the initially demagnetized point. This phenomenon was unexpected since some residual magnetic force was expected to be remaining from the previous test. It is speculated that the reason for this phenomenon stems from the fact that the solenoid plunger location had to be adjusted prior to commencement of each test. Thus mechanical work produced by moving the plunger generated back emf that was dissipated in the form of core losses.

As seen from figures 2.4 through 2.6, the force produced by the solenoid at any given excitation current is not unique, but rather dependent on the history of the coil current excursion (the effect of a memory element in the ferromagnetic medium). This phenomenon implies that the solenoid transfer characteristics are time-varying. However, the hysteresis effects were mild and thus were neglected in this design. Thus, for the purposes of establishing a static time-invariant memoryless algebraic dependency known as the defining equation, the force readings at a given plunger position and coil current over the five sweeps of programming current from 0A to 3A and back to 0A, were averaged.

The measurements presented in table 2.1 represent the averaged force reading at a given displacement and excitation current and 3-dimensional graphic representation is given in figure 2.7.

Displacement

I(A)	0.00254 meters	0.00381 meters	0.00508 meters	0.00762 meters	0.01016 meters	0.01270 meters	0.01524 meters	0.01778 meters	0.0203 meters
0.20A	0.61	0.38	0.16	0.14	0.11	0.14	0.04	0.07	0.03
0.40A	2.28	0.83	0.82	0.52	0.37	0.22	0.20	0.18	0.11
0.60A	4.82	2.35	1.97	1.16	0.76	0.48	0.48	0.39	0.25
0.80A	8.39	4.46	3.01	2.01	1.31	0.92	0.82	0.65	0.46
1.00A	12.67	6.98	5.61	3.13	2.00	1.43	1.24	0.96	0.71
1.20A	17.63	10.11	7.42	4.48	2.82	2.04	1.73	1.36	1.03
1.40A	22.32	13.63	9.84	6.11	3.86	2.75	2.30	1.82	1.35
1.60A	25.88	17.26	12.77	7.91	4.98	3.57	2.90	2.27	1.74
1.80A	29.47	20.67	17.11	9.85	6.23	4.46	3.59	2.79	2.17
2.00A	29.95	23.87	18.43	11.69	7.51	5.45	4.28	3.28	2.60
2.20A	34.11	26.71	21.83	14.52	9.28	6.67	5.08	3.88	3.19
2.40A	36.45	29.31	24.70	16.90	11.09	7.94	6.07	4.61	3.77
2.60A	38.68	31.69	27.44	19.30	12.94	9.30	7.03	5.42	4.42
2.80A	40.82	33.60	29.80	21.68	14.85	10.76	8.19	6.31	5.08
3.00A	42.34	35.95	32.13	23.82	16.75	12.31	9.44	7.36	5.93

Force (Newtons)

Table 2.1 Steady-State Measurement Results

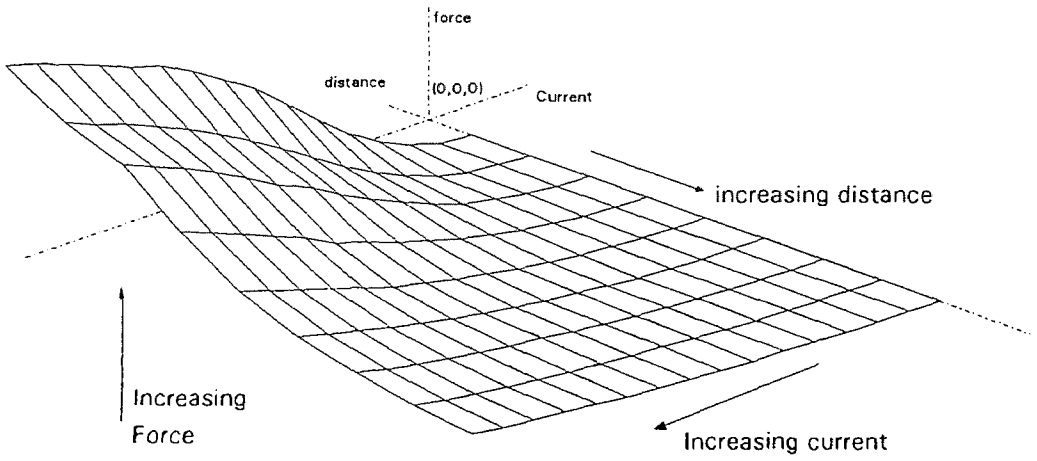

Figure 2.7 Graphic Representation of Steady-State Measurements

2.2.3 Dynamic Characteristics Measurements

The high frequency small signal hysteresis has a noticeable effect on the actuator dynamics. There is obviously a core loss that is proportional to frequency and the amplitude of the alternating flux, as well as the phase shift and lower effective gain that ascents from the nonlinear attributes of the hysteresis.

The phase shift and small signal gain reduction associated with the minor hysteresis loop vary with frequency and plunger displacement and not with DC operating current. Some subtle variations may occur with excitation signal amplitude variation; however, the general shape of the loop will remain the same and only the core loss parameters will be effected. Thus, for accurate dynamic nonlinearities identification it is sufficient to collect the phase shift and gain data at arbitrary bias current at different displacement settings with small excitation component.

The data of interest were obtained with the help of the Model 5060A Frequency Response Analyzer manufactured by NL Electronic Interments using the setup depicted in figure 2.3.

Two typical frequency response plots are shown in figures 2.8 and 2.9. The small signal force gain and phase were measured over the frequency span of 0.1Hz to 1000Hz. The useful frequency range of the collected data was restricted by the inherent limitations of the thin beam load cell measuring technique. The second order resonant pole located at approximately 200Hz was induced by the thin beam resonance rendering the force measurements at frequencies above its resonance unusable.

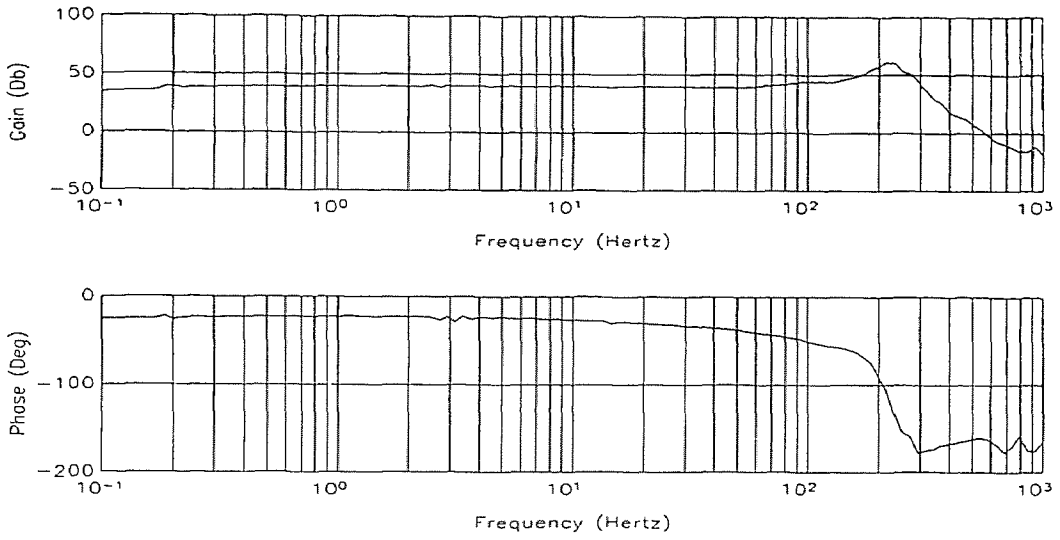

Figure 2.8 Hysteresis Effects at 2ADC, 0.2" (0.00508m) Displacement

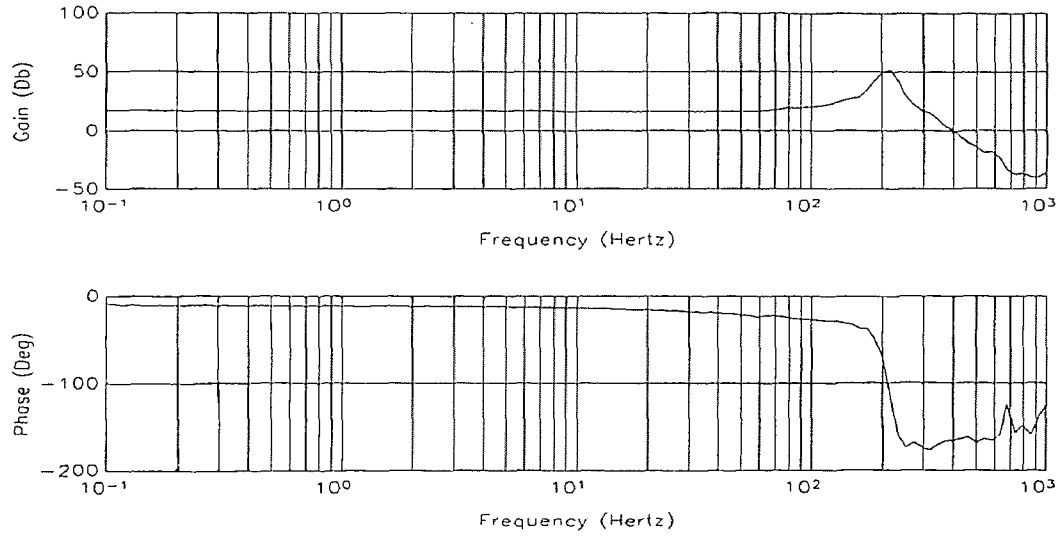

Figure 2.9 Hysteresis Effects at 1ADC, 0.5" (0.0127m) Displacement

Measurements presented in figure 2.8 were obtained around the 2 Ampere operating point with the plunger position fixed at 0.2' (0.00508m). The average phase shift over the frequency span from 0.1 to 100 Hz was -28° and the average dynamic gain for the same frequency range was 25.1dB.

The expected small-signal gain may be calculated by evaluating the derivative of the equation 2.7 at the operating point. The predicted small-signal gain for given operating point is 29.29dB, which implies that the small-signal gain reduction due to the hysteresis is 4.19dB.

Similarly, for the small-signal measurements at 1 Ampere operating point with 0.5" (0.0127m) plunger displacement (figure 2.9), the average phase shift was measured at 11° and gain reduction was 2.34dB.

Further tests returned similar results. The phase shift no more than 30° and maximum gain reduction of 5.7dB was observed .

2.3 Establishing Defining Equation

2.3.1 Optimization Procedure

For implementation of the feedback linearization control algorithm the expression for the *solenoid current that will produce the desired force at a given displacement* is required, while for an Observer implementation the *force output as a function of excitation current and displacement* is of interest. This section concentrates on the defining the static describing equation that is compliant with data in table 2.1.

It stands to reason that a general expression describing the behavior of actual solenoid will stem from the derivation in section 2.1.1, thus from equation 2.2

$$i = \sqrt{f \cdot \frac{d^2}{k}} \qquad \text{where} \quad k = -\frac{\mu_0 N^2}{2}$$

Intuitively, the actual device should follow the same basic dependency, i.e.

$$i = \sqrt{g(f) \cdot h(d)}$$

where *g(f)* and *h(d)* is a polynomial function of force and distance respectively. Obviously, it is not essential for the functions to be polynomial; however, polynomial functions are preferred because they are least computationally intensive.

The polynomial coefficients of *g(f)* and *h(d)* may be selected by a suitable numerical means to fit the measured data.

Matlab's "Constr.m" routine is ideally suited for this application. **X=constr("FUN",X0)** starts at **X0** and finds a constrained minimum to the function which is described in FUN (usually an M-file: FUN.M). The function **"FUN"** is designed to return two arguments: a scalar value of the function to be minimized, **F**, and a matrix of constraints, **G**: **[F,G]=FUN(X)**. **F** is minimized such that **G < zeros(G)**.

If the measured data are arranged in a *n* by *m* matrix as shown in table 2.1 such that each of *m* columns corresponds to the force measurements obtained at a fixed distance, and each of *n* rows corresponds to the force measurements obtained at a fixed current, the function to be minimized is the least squares error that is defined as:

$$LSError = \sum_{i=1}^{m}\sum_{j=1}^{n}\left(\frac{I_j - I(f_j,d_i)}{I_j}\right)^2 \tag{2.3}$$

where $I(f_j,d_i)$ is the solenoid current that produces the desired force at a given displacement . Logically, the selected polynomial coefficients must be such that *g(f)* and *h(d)* are positive. Thus the constraint factor for the "Constr.m" routine is the sign of *g(f)* and *h(d)*.

It is desirable to select the simplest defining equation that will furnish a reasonable result. An increase in the polynomial order of *g(f)* and *h(d)* will reduce the least squares error at the cost of CPU calculation time, thus an intelligent tradeoff must be made between describing equation accuracy and its complexity. The order of $g(f)_{ideal}$ and $h(d)_{ideal}$ for the ideal solenoid is 1 and 2 respectively. It is expected that the describing equation for the actual device is more complex, therefore a polynomial of higher order was selected for *g(f)* and *h(d)* so that

$$i = \sqrt{(K_1 f^2 + K_2 f)\cdot(K_3 d^3 + K_4 d^2 + K_5 d + K_6)} \tag{2.4}$$

A Matlab file "Get_LSE.m" (Get Least Squares Error) was generated to be used in conjunction with "Constr.m" routine and is listed in table 2.2. This script file contains the program code to calculate the least squares error as defined by equation 2.3 for the equation of form shown in equation 2.4 with given set of coefficients K_1 through K_6. The constraining factors are the signs of *g(f)* and *h(d)*.

```
function [LSError,Q,Error]=Get_LSE(K)          % (Get Least Squares Error)
load force;                                    % file containing Force, I , and D matrices
LSError=0;
Q=-1e-6*[1 1];
[m,n]=size(Force);
for k=1:m
 for l=1:n
  gf=K(1)*Force(k,l)^2+K(2)*Force(k,l);        % calculate g(f)
  hd=K(3)*D(l)^3+K(4)*D(l)^2+K(5)*D(l)+K(6);   % calculate h(d)
  i=(abs(gf*hd))^.5;
  error=(I(k)-i)/I(k);
  LSError=LSError+(error)^2;
  if gf < 0,                                   % Constraint 1  g(f) must be positive
    Q(1)=Q(1)-gf;
  end;
  if hd < 0,                                   % Constraint 2  h(d) must be positive
    Q(2)=Q(2)-hd;
  end;
 Error(k,l)=error;
 end;
end;
```

Table 2.2 Matlab Routine Used for Curve Fitting

Implementation of "Constr.m" routine also requires an estimate of a starting point (**X0**). A successful selection of a starting point usually means more than shorter optimization routine execution time. A random starting point will often send the numerical optimization routine in search of a local rather then the absolute minima.

Measured data and basic knowledge of the system characteristics provide the means of selecting a reasonable starting point. It may be assumed for the purposes of obtaining a starting point that behavior of the electromagnet resembles the behavior of the ideal device who's defining equation is $i = \sqrt{f \cdot \frac{d^2}{k}}$, then the initial coefficients of equation 2.4 describing the behavior of the actual device are $K_1 = K_3 = K_5 = K_6 = 0$, $K_2 = 1$, and $K_4 = 1/k$. The value for $K_4 = 1/k$ is readily obtained from a distinct measured data sample selected from table 2.1. For example, the force measurement at displacement $d = 0.0127$ meters and current $i = 2$ Amperes was measured to be 5.45 Newtons, thus $2A = \sqrt{5.45N \cdot (0.0127)^2 / k}$, hence $K_4 = 1/k = 4550.5$.

2.3.2 Optimization Results

With given starting point, the **"constr("Get_LSE",XO)"** command returned an optimal set of coefficients in less than 400 iterations. The describing equation based on the polynomial coefficients selected by the optimization routine is

$$i = \sqrt{(0.0103f^2 + 0.472f)\cdot(-0.0073d^3 + 4550.5d^2 + 41.7d + 0.0198)} \qquad (2.5)$$

Equation 2.5 was further simplified by eliminating the d^3 term and normalizing all coefficients with respect to the f^2 term. The d^3 term coefficient is six orders of magnitude lower than the coefficient of the d^2 term , therefore omitting this term had negligible effect on the accuracy of the defining equation. Normalizing coefficients with respect to the f^2 term saves one computation step and scales the remaining equation constants more favorably.

Using the scaled coefficients from the previous optimization run as the starting point for the new search routine, the optimization process was repeated. As expected, the least squares error produced by the simplified equation was virtually unchanged.

Based on the output of the second optimization , the simplified defining equation is

$$i = \sqrt{(f^2 + 45.669f)\cdot(47.003d^2 + 0.4312d + 0.000204)} \qquad (2.6)$$

and the defining expression for force is

$$f = \sqrt{521.423 + \frac{i^2}{47.003d^2 + 0.4312d + 0.000204}} - \sqrt{521.423} \qquad (2.7)$$

Table 2.3 is the matrix of error coefficients where the error coefficient is defined as

$$Error(i,j) = \left(\frac{I_j - I(f_j, d_i)}{I_j} \right) \cdot 100\% \qquad (2.8)$$

The average error of the Error matrix is just under 4%. This is a very encouraging result considering the fact that typical lot variations for a given device exceed 10% .

Displacement

I(A)	0.00254 meters	0.00381 meters	0.00508 meters	0.00762 meters	0.01016 meters	0.01270 meters	0.01524 meters	0.01778 meters	0.0203 meters
0.0A	0	0	0	0	0	0	0	0	0
0.20A	-6.32	-5.53	18.03	-0.65	-9.86	-46.98	9.36	-35.96	0.61
0.40A	-4.55	21.72	7.12	3.55	0.35	7.79	-1.52	-9.14	4.75
0.60A	-4.04	10.89	2.99	3.20	3.70	9.90	-4.07	-5.95	4.12
0.80A	-6.60	5.98	9.16	3.46	4.72	5.52	-2.84	-3.42	3.31
1.00A	-8.84	3.58	5.32	2.55	5.11	5.41	-1.42	-0.60	3.26
1.20A	-11.44	0.42	0.68	1.49	5.26	5.27	-0.29	-0.53	2.83
1.40A	-11.41	-2.13	-0.24	-0.16	4.05	5.02	0.29	-0.08	4.10
1.60A	-7.67	-3.59	-2.56	-1.43	3.59	4.63	1.42	1.80	4.46
1.80A	-4.65	-3.46	-7.17	-2.42	2.97	4.34	1.78	2.54	4.56
2.00A	-0.58	-2.44	-3.22	-2.07	2.94	3.93	2.79	4.46	5.63
2.20A	5.07	-0.52	-4.78	-5.96	0.31	2.24	2.92	4.97	4.41
2.40A	8.75	1.77	-4.34	-6.83	-1.52	1.04	1.82	4.33	4.19
2.60A	12.05	4.22	-3.45	-7.38	-2.86	-0.12	1.53	3.56	3.61
2.80A	15.05	7.29	-1.73	-7.63	-3.98	-1.34	0.24	2.49	3.41
3.00A	18.54	9.18	-0.09	-6.93	-4.68	-2.52	-1.12	0.75	1.75

Error (%)

Table 2.3 Error Coefficients Matrix from Optimization Results

2.4 Parameter Identification Summary

The parameter identification study of the D-Frame Intermittent duty Solenoid Electromagnet Part No. 53719-87 manufactured by Deltrol Controls has determined the static defining equation describing solenoid's behavior as

$$f = \sqrt{521.423 + \frac{i^2}{47.003d^2 + 0.4312d + 0.000204}} - \sqrt{521.423}$$

where f is the force developed by the solenoid, i is the coil excitation current, and d is the solenoid plunger displacement referenced to the completely seated position.

The expression for the solenoid current that will produce the desired force output at a given displacement is the inverse or the linear transformation expression was found to be

$$i = \sqrt{(f^2 + 45.669f)\cdot(47.003d^2 + 0.4312d + 0.000204)}$$

Memory element due to the large signal low frequency excitation is presented in figures 2.4 through 2.5.

Under small-signal dynamic excitation the solenoid exhibits hysteresis related secondary effects such as phase shift and dynamic gain reduction. The maximum gain reduction is just under 6dB and phase lag is below 30°.

CHAPTER 3

CONTROLLING THE NONLINEAR PLANT

3.1 Nonlinear Control Algorithm

The *feedback linearization* method was selected to control the single-axis agonistic plant. The basic intent of the feedback linearization method is to transform the state and control variables of the plant to another set of state and control variables, such that the dynamics of the transformed system are linear. Linear design techniques then used to obtain a suitable control law, and finally, transformation is inverted to get the control law back to the original state and control variables .

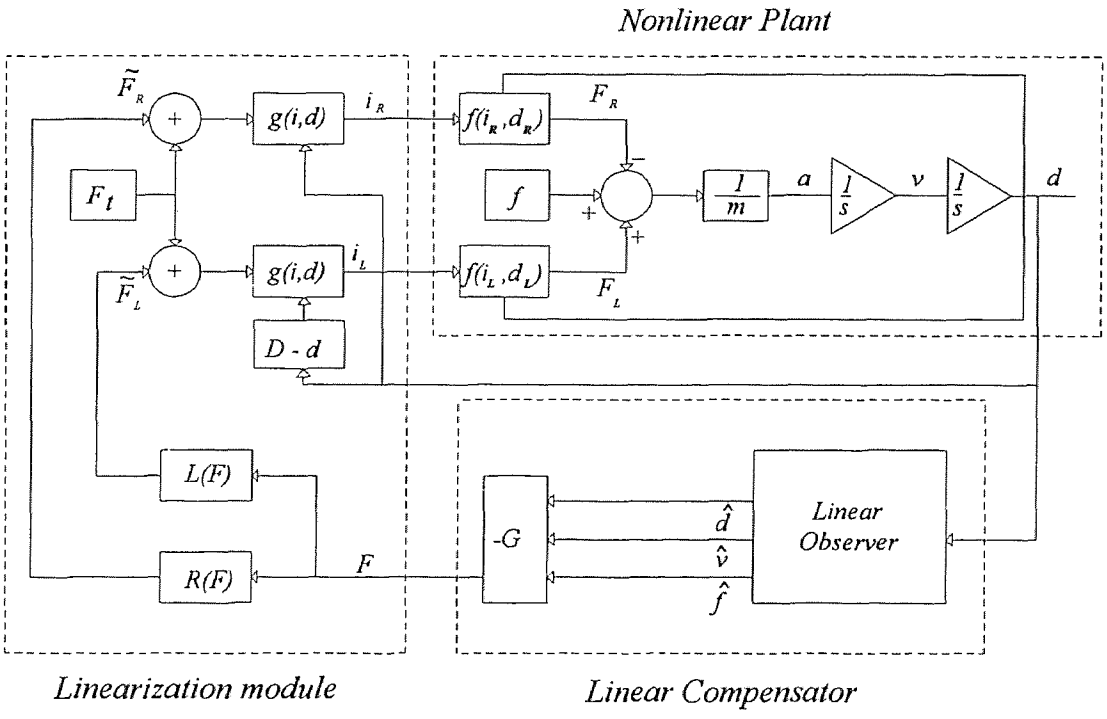

Figure 3.1 Block Diagram, Feedback Linearization Implementation

Figure 3.1 is the block diagram of the feedback linearization control law applied to the solenoid-driven agonistic plant.

The control inputs to the nonlinear plant are the excitation currents in the left and right solenoids (i_L and i_R) and the output is the payload position d. The currents in each solenoid produce force that acts on the payload in opposing directions. Thus, the payload is propelled by the force that is the arithmetic difference between the two opposing forces produced by the left and right solenoids, and restrained by an exogenous input force f introduced by the friction. The function blocks denoted by $f(i,d)$ represent the solenoid defining equation approximated by equation (2.7).

The nonlinear control variables i_L and i_R are transformed to a linear set of variables in the linearization module. In case of the agonistic plant with solenoid electromagnet actuator, the nonlinear control variable is the solenoid excitation current and the transformation control variable is the force. The linear transformation that cancels nonlinearity inherent to solenoid electromagnet thus resulting in linearized control system was developed in section 2.3.2 and repeated in equation 3.1.

$$i = \sqrt{(f^2 + 45.669f)\cdot(47.003d^2 + 0.4312d + 0.000204)} \qquad (3.1)$$

Equation 3.1 is the expression for the *solenoid current that will produce the desired force output at a given plunger displacement.*

The variables to be controlled in agonistic plant are the *payload position*, d, and the *tension* in the tendons. The major advantage of the feedback linearization method is

characteristic to the agonistic control approach. With feedback linearization the individual solenoid forces are known, thus the tendon tension may be preset algebraically with no augmented dynamics. This characteristic is demonstrated in figure 3.2. where function *g(i,d)* represents the linear transformation equation given by (3.1).

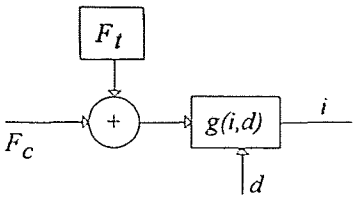

Figure 3.2 Tension Control

To assure that the tension in the tendon driven by a solenoid does not fall below a specified minimum, it is sufficient to sum the nonnegative control force F_c created by the linear regulator with a constant tension force F_l. The control force F_c is clearly nonnegative because the force produced by the solenoid acts only in the direction of decreasing plunger displacement.

With feedback linearization module in place, and intrinsic tension control, the dynamics of the linearized system reduce to a pure mass dynamics with one control variable where

$$\ddot{d} = \frac{F}{m} \tag{3.2}$$

The net force acting on the payload F is defined as $F = F_L - F_R$ where F_R and F_L are the forces developed by the right and left solenoid respectively. A linear control law for the linearized agonistic plant is developed in Chapter 4.

With a single control variable the linearization algorithm must distribute the control force between the left and right solenoids. Figure 3.3 shows how the forces in each solenoid were partitioned. This force distribution was chosen because the solenoid is an absolute value device as seen from the defining equation 2.6 where regardless of the polarity of the applied current the direction of the generated force is unchanged.

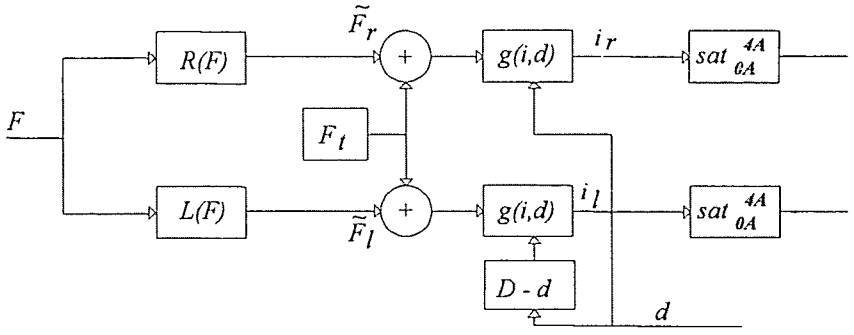

Figure 3.3 Expanded Block diagram of Linearization Module

The functions $L(F)$ and $R(F)$ are the limiters that are defined as follows

$$L(F) = \begin{cases} F & for \ F > 0 \\ 0 & for \ F \le 0 \end{cases} \quad \text{and} \quad R(F) = \begin{cases} -F & for \ F < 0 \\ 0 & for \ F \ge 0 \end{cases} \tag{3.3}$$

thus, a positive control force drives the left solenoid while the negative control actuates the right solenoid.

The payload position d is measured with reference to the right solenoid, thus the displacement input to the linearization equation for the right solenoid uses the feedback directly, while the displacement input to the left solenoid is obtained from $d_L = D - d$ where D is the total travel distance.

The linearization module is used to protect the actuators and power amplifiers from inevitable overloads. As a safeguard, a saturation function was placed on the current outputs. The lower limit was set to zero and the high limit to 4 Amperes.

3.2 Actuator Saturation and Windup

An adverse effect attributed to actuator saturation is the integrator windup. In the next section a linear observer that produces a controller with an integral action is designed. The integral action is needed to assure zero steady-state error. Unless the actual force output is used as an input to the observer, the controller integral stage will tend to overcompensate resulting in inferior large signal performance.

The windup attributes are corrected by using the *actual* output force as an input to the observer. The actual solenoid output force for each solenoid is computed in accordance with equation 2.7 and the real net force acting on the payload is the algebraic difference between the force produced by the left and right solenoids. The effects of friction for this calculation were ignored because of the large differences between the 1.25 Newton friction and typical 20 Newton saturation force.

3.3 Effects of Sampling on Linearization Algorithm

The feedback linearization method assumes a continuous transformation process such that at any given time the current that will produce the desired force output at a given displacement is available. However, in the presence of computational delay, the solenoid plunger displacement information will lag the actual position.

For example, if the payload is moving at the speed of 5 m/sec (this corresponds to 40 millisecond transition over full travel distance of 2 cm) , the 0.8 milliseconds computation delay will translate into a position feedback error for the linearization calculation of 4 mm thus imbedding a 20% error in the actual plunger displacement measurement.

This problem is simply handled. With available velocity estimate the actual displacement at the time of output is simply

$$d(t+t_d) = d + v \cdot t_d \tag{3.4}$$

CHAPTER 4

LINEAR CONTROLLER DESIGN

In this chapter a linear controller for the linearized single-axis agonistic plant is designed and simulated. The controller consists of a Linear Quadratic regulator and Kalman Filter based observer

The controller is designed using the direct discrete-time approach to assure that the compensator design exactly includes the digitizing effects of Zero Order Hold (ZOH) properties, and sampling period limitations. In direct discrete design of digital controllers, the continuous-time plant is first discretized, then the controller is designed for the discrete-time system [3]. In paragraphs 4.1 and 4.2 the continuous-time system is described and then converted into a sampled system. The compensator design is performed in discrete-time, however, since sampled and continuous-time weighting matrices are closely related, the effect of the weighting matrices on the closed-loop pole location is examined in continuous-time.

The optimization procedure is presented in paragraph 4.3. The optimization is done numerically with the Matlab's "constr.m" routine [8]. The routine is programmed to select the best set of LQR coefficients to minimize the step response overshoot given a minimum sampling rate and upper and lower closed-loop natural frequency bounds.

4.1 Continuous-Time Analysis

4.1.1 Optimal Linear Quadratic Regulator

For a general linear dynamic plant in the presence of exogenous input

$$\begin{aligned} \dot{x} &= Ax + Bu + Ex_0 \\ y &= Cx + Du \end{aligned} \tag{4.1}$$

a linear Full State Feedback control law has a following form

$$u = -Gx - G_0 x_0 \tag{4.2}$$

where x_0 is the vector of exogenous variables assigned for modeling friction and other unmodeled parameters.

The state gain matrix G is usually obtained by solving the Optimal Linear Quadratic Regulator problems so that

$$G = R^{-1}B^T M \tag{4.3}$$

where M is a symmetric positive definite matrix that satisfies the algebraic Riccatti equation

$$0 = MA + A^T M - MBR^{-1}B^T M + Q \tag{4.4}$$

The exogenous input gains are obtained directly from

$$G_0 = B^{\#}E \tag{4.5}$$

where matrix $B^{\#}$ is a left pseudo inverse of B. In the special case where B and E matrices are identical the G_0 is the identity matrix.

The state space equations for the linearised antagonistic plant are

$$\begin{aligned} \dot{d} &= v \\ \dot{v} &= \frac{1}{m}F + \frac{1}{m}f \end{aligned} \tag{4.6}$$

where d is the payload displacement, v is the velocity, F is the net force acting on the load (i.e. $F = F_{right} - F_{left}$), and f is the exogenous force.

Defining the state vector as $x = \begin{bmatrix} d & v \end{bmatrix}^T$ the state matrices the linearised antagonistic plant are

$$A = \begin{bmatrix} 0 & 1 \\ 0 & 0 \end{bmatrix} \qquad B = E = \begin{bmatrix} 0 \\ \left(\frac{1}{m}\right) \end{bmatrix} \qquad C = \begin{bmatrix} 1 & 0 \end{bmatrix}, \text{ and } \quad D = \begin{bmatrix} 0 \end{bmatrix} \tag{4.7}$$

According to (4.2) the control law for the system described by (4.7) has the following form

$$F = -g_d d - g_v v - f \tag{4.8}$$

Note that the exogenous term coefficient is unity since B and E matrices are identical.

The characteristic equation for system described by (4.7) is

$$|sI - A + BG| = s^2 + s\frac{g_v}{m} + \frac{g_d}{m} \tag{4.9}$$

Its characteristic equation roots are located at

$$s_1, s_2 = \frac{g_v}{2m} \pm \sqrt{\left(\frac{g_v}{2m}\right)^2 - \frac{g_d}{m}} \tag{4.10}$$

It can be readily shown that characteristic roots in the location $s_1, s_2 = -a \pm jb$ may be also obtained by the solution of the optimal linear quadratic regulator as defined in (4.3) and (4.4) provided that the weighting matrices are selected such that

$$R = I \quad \text{and} \quad Q = \begin{bmatrix} (a^2 + b^2)m & 0 \\ 0 & 2m^2(a^2 - b^2) \end{bmatrix} \tag{4.11}$$

Since matrix Q must be positive semi-definite, the limiting condition on root location selection is that $a > b$.

4.1.2 Kalman Filter Based Observer

For a given a dynamic plant

$$\begin{aligned} \dot{x} &= Ax + Bu + Fv \\ y &= Cx + w \end{aligned} \tag{4.12}$$

where v and w are white noise processes with known spectral density the optimum observer can be expressed by

$$\dot{\hat{x}} = A\hat{x} + Bu + K(y - C\hat{x}) \tag{4.13}$$

In the case where the process and measurement noise are not correlated the optimal steady-state gain matrix K is given by

$$K = PC^T W^{-1} \tag{4.14}$$

where the optimizing covariance matrix P satisfies the algebraic matrix Riccati equation

$$0 = AP + PA^T - PC^T W^{-1} CP + FVF^T \tag{4.15}$$

The linear observer was used in this project to compensate for the nonlinear effects of friction. The method of simultaneously estimating and canceling friction is based on the Coulomb friction model where the friction force is constant in magnitude and changes sign to oppose velocity.

Assuming that the exogenous force is a Wiener process given by $\dot{f} = q$ where q is the white noise with spectral density matrix V, the resulting compensator based on the observer that estimates this parameter will have integral control action, with the gain in the integral control path that is proportional to assumed level of friction [2].

The state space equations for the linearized agonistic plant in the presence of Weiner process may be written as

$$\begin{aligned} \dot{d} &= v \\ \dot{v} &= \frac{F}{m} + \frac{f}{m} \\ \dot{f} &= q \end{aligned} \tag{4.16}$$

with observation equation

$$y = d + w \tag{4.17}$$

where w is the measurement noise with spectral density matrix W that is assumed to be white.

The defining matrices for this system are

$$A = \begin{bmatrix} 0 & 1 & 0 \\ 0 & 0 & \frac{1}{m} \\ 0 & 0 & 0 \end{bmatrix} \quad B = \begin{bmatrix} 0 \\ \left(\frac{1}{m}\right) \\ 0 \end{bmatrix} \quad F = \begin{bmatrix} 0 \\ 0 \\ 1 \end{bmatrix} \quad C = \begin{bmatrix} 1 & 0 & 0 \end{bmatrix} \tag{4.18}$$

If the process and measurement spectral density matrices are

$$V = (\Omega^3 \cdot mass)^2$$
$$W = I \tag{4.19}$$

where

$$\Omega = \left(\frac{V}{W \cdot mass^2} \right)^{1/6} \tag{4.20}$$

the solution of the Algebraic Riccatti Equation (4.15) yields the gain matrix K such that the characteristic roots are positioned at

$$s_1 = -\Omega$$
$$s_2 = -\Omega \left(\frac{1}{2} \pm j\sqrt{\frac{3}{2}} \right) \tag{4.21}$$

This is a characteristic "Butterworth pattern" where the roots lie upon a circle of radius Ω on the negative real axis and at 60° angles [1].

If the Butterworth pattern is not desirable due to its lightly damped nature, the pole location pattern may be adjusted by appending additional weighting on all state variables. However, this modification complicates the analytic derivation thus future weighting parameter variations will be left to numerical means. Meanwhile, the process and measurement spectral density matrices of equation (4.19) that produce the Butterworth pattern, provide reasonable starting point for numerical optimization algorithm.

4.2 Linear System Discretization

The controller for the linearized agonistic plant was designed using the direct discrete-time approach to assure that the compensator design exactly includes the digitizing effects such as Zero Order Hold (ZOH) properties, and sampling period limitations. In the direct discrete design procedure of digital controllers, the continuous-time plant is first discretized, or converted into a sampled system, then a controller is designed for the discrete-time system.

The continuous-time plant as seen by the Digital Signal Processor (DSP) is shown in figure 4.1. The output information $y(k)$ is obtained by sampling the plant output $y(t)$ at time $t = kT$ where T is the sampling period. It is customary to hold the control input $u(t)$ constant between control switching. This effect is implicit in real-time control application and is contributed by a ZOH on the controller output.

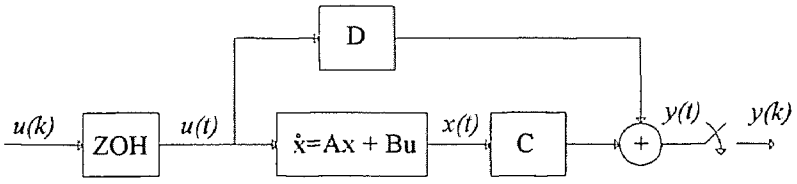

Figure 4.1 Real-Time Continuous Plant Interface

The continuous time-invariant plant given by

$$\begin{aligned} \dot{x} &= Ax + Bu \\ y &= Cx + Du \end{aligned} \tag{4.22}$$

is seen by DSP in discretized form [3] as

$$\begin{aligned} x_{k+1} &= A_s x_k + B_s u_k \\ y_k &= C x_k + D u_k \end{aligned} \tag{4.23}$$

where A_S and B_S are the sampled equivalents of state matrices A and B and defined as

$$\begin{aligned} A_s &= e^{AT} \\ B_s &= \int_o^\tau e^{AT} B \, d\tau \end{aligned} \tag{4.24}$$

4.2.1 Kalman Filter Discretization

Using the Discretization procedures outlined in (4.23) and (4.24), the sampled Kalman filter equivalent of (4.18) is obtained.

$$A = \begin{bmatrix} 1 & T & \left(\frac{T^2}{2mass}\right) \\ 0 & 1 & \left(\frac{T}{mass}\right) \\ 0 & 0 & 1 \end{bmatrix} \quad B = \frac{1}{m}\begin{bmatrix} \left(\frac{T^2}{2}\right) \\ T \\ 0 \end{bmatrix} \quad F = \begin{bmatrix} \left(\frac{T^3}{6mass}\right) \\ \left(\frac{T^2}{2mass}\right) \\ T \end{bmatrix} \tag{4.25}$$

The discrete version of a continuous time Kalman filter has the following form

$$\hat{x}_{\bar{k}+1} = A\hat{x}_{\bar{k}} + Bu_k + AK_k(y_k - C\hat{x}_{\bar{k}}) \tag{4.26}$$

where $\hat{x}_{\bar{k}}$ is defined as the estimate at time k just before the measurement y_k is obtained and K_k is the vector of optimal discrete Kalman filter gain coefficients [3]. The gain matrix subscript $(\cdot)_k$ denotes the fact that the optimal gain computation is conceivable on line, however for a system of moderate complexity it is advantageous to compute these coefficients prior to implementation. The estimate at time $k+1$ is

$$\hat{x}_{k+1} = \hat{x}_{\bar{k}+1} + K(y_{k+1} - C\hat{x}_{\bar{k}+1}) \tag{4.27}$$

The above Kalman filter formulation is known as the *recursive apriori formulation*. It provides a predictive estimate $\hat{x}_{\bar{k}+1}$ of $\hat{x}_{k+1}$ one sampling period in the future, in that the most current measurement y_{k+1} is not used. Thus the filter automatically has a computational delay T built in, making it unnecessary to include an extra state to model a fractional time delay.

The scalar form of the sampled steady-state Kalman filter for the agonistic control plant shown in 4.28 is obtained by substituting (4.25) into (4.26).

$$\begin{aligned}
\hat{d}_{k+1} &= \hat{d}_k + T\hat{v}_k + \frac{T^2}{2m}\left(\hat{f}_k + F_k\right) + L_1\left(y_k - \hat{d}_k\right) \\
\hat{v}_{k+1} &= \hat{v}_k + \frac{T}{m}\left(\hat{f}_k + F_k\right) + L_2\left(y_k - \hat{d}_k\right) \\
\hat{f}_{k+1} &= \hat{f}_k + L_3\left(y_k - \hat{d}_k\right)
\end{aligned} \tag{4.28}$$

with filter gains L_i given by

$$\begin{bmatrix} L_1 \\ L_2 \\ L_3 \end{bmatrix} = \begin{bmatrix} K_d + K_v T + K_f \dfrac{T^2}{2m} \\ K_v + K_f \dfrac{T}{m} \\ K_f \end{bmatrix} \tag{4.29}$$

where K_d, K_v, K_f are the displacement, velocity and exogenous force optimal Kalman filter gains that are calculated off-line.

4.2.2 Linearized Agonistic Plant Discretization

It is readily shown that the discretized equivalents of the linear continuous plant defined in (4.7) are

$$A_s = \begin{bmatrix} 1 & T \\ 0 & 1 \end{bmatrix} \quad \text{and} \quad B_s = \frac{1}{m}\begin{bmatrix} (T)^2/2 \\ T \end{bmatrix} \tag{4.30}$$

It should be noted that the computational delay compensation was not required since the compensator includes an observer with recursive apriori formulation.

4.3 Selecting Optimal Parameters

In this section the numerical optimization techniques are used to select the best LQR coefficients to minimize the step response overshoot given a minimum sampling rate and upper and lower closed-loop natural frequency bounds.

Matlab's "Constr.m" routine was used to perform this task. The command **X=constr("FUN",X0)** starts at **X0** and finds a constrained minimum to the function which is described in FUN (usually an M-file: FUN.M). The function **"FUN"** is a user written program designed to return two arguments, a scalar value of the function to be minimized, **F**, and a matrix of constraints, **G: [F,G]=FUN(X)**. **F** is minimized such that **G < zeros(G)**.

Table 4.1 is the listing of the Matlab's script file MinOver.m that was designed to be used in conjunction with the "constr.m" routine. As its name implies, the variable to be minimized is the maximum output overshoot caused by a step programming excitation.

4.3.1 Optimization Constraints

Three constraint factors were imposed on the optimization . The minimum sampling time was restricted to 0.8 milliseconds. The restriction was based on the maximum measured execution time of the program on the given computer. The maximum closed-loop natural frequency was restricted to 1000 rad/sec which is approximately 1/4 of the Nyquist rate. The minimum closed-loop natural frequency was limited to 100 rad/sec.

```
function [J,G]=MinOver(K);
%-------------------------------------------------------------------------%
% This function is designed to be used with 'constr.m' routine
% to optimize the overshoot of the closed-loop agonistic system
%-------------------- Define constants ---------------------------------%
T=abs(K(9));
mass=.36877;       % Payload mass in Kg
%----------------- Performance Constraints ----------------------------%
MinW  = 100;              % Minimum acceptable damping
MaxW =  1000;             % Maximum natural frequency
MinT  =  0.8e-3;          %  Minimum Sampling Period
%------------------------------- Kalman Filter ---------------------------%
Afs=[1 T T^2/2/mass;0 1 T/mass;0 0 1];
Bfs=1/mass*[T^2/2;T;0];
Ffs=[T^3/6/mass 0 0;0 T^2/2/mass 0;0 0 T];
Cfs=[1 0 0];
V=[K(3) K(4) K(5);K(4) K(6) K(7);K(5) K(7) K(8)];
V=V*V';
W=1;
[Kfs,Ss,P,Efs]=dlqe(Afs,Ffs,Cfs,V,W);
%---------------------------- FSFB compensator ------------------------%
Acs = [1 T;0 1];
Bcs = 1/mass*[(T^2)/2;T];
Qcs = [K(1) 0 ;0 K(2)];
Qcs=Qcs*Qcs';
Rcs=1;
[Gcs,Ms,Ecs]=dlqr(Acs,Bcs,Qcs,Rcs);
%------------------- Augmented System Matrices ----------------------%
Ge = [Gcs 1 0 0];
Aas = [(Afs-Afs*Kfs*Cfs) zeros(3,2);zeros(2,3) (Acs)];
Aas= Aas - [Bfs;Bcs]*Ge*[eye(3)-Kfs*Cfs zeros(3,2);zeros(2,3) eye(2)];
Bas = [Afs*Kfs;zeros(2,1)]-[Bfs;Bcs]*Ge*[Kfs;zeros(2,1)];
Cas = [0 0 0 1 0 ];
Das = 0;
%------------------ Determine Performance parameters ----------%
[Y,X]=dstep((Aas+Bas*Cas),-Bas,Cas,0);
[mag,wn,z] = ddamp((Aas-Bas*Cas),T);
%------------------------- Performance index ----------------------------%
J =  max(Y);                % Optimizing for lowest overshoot
%--------------------------- Constraints ----------------------------------%
G(1) = MinW - min(wn) ; %  Minimum natural frequency
G(2) = max(wn) - MaxW; % Maximum natural frequency
G(3)=  MinT -T;             % Minimum sampling rate
```

Table 4.1 Matlab Code MaxOver.m

4.3.2 Function MimOver.m

The function MinOver.m was written to be used in conjunction with "constr.m" routine to optimize the overshoot of the closed-loop agonistic system.

The input argument to the MinOver.m function is a vector of variables (X) selected by the "constr.m" routine. There are nine variables in given control problem. Two variables are needed for the state weighting matrix (Q) that controls the location of the closed-loop poles contributed by the Linear Quadratic Regulator. Thus

$$Q = \hat{Q}\hat{Q} \qquad \text{where } \hat{Q} = \begin{bmatrix} X(1) & 0 \\ 0 & X(2) \end{bmatrix} \tag{4.31}$$

To control the pole locations contributed by the Kalman Filter, all entries of the noise covariance matrix (V) must be varied. Keeping in mind that matrix V must be symmetrical, six variables are needed to gain full control over the third order observer pole location. The Noise covariance matrix variables were distributed as follows:

$$V = \hat{V}\hat{V} \qquad \text{where } \hat{V} = \begin{bmatrix} X(3) & X(4) & X(5) \\ X(4) & X(6) & X(7) \\ X(5) & X(7) & X(8) \end{bmatrix} \tag{4.32}$$

Note that Q and V matrices are used for the solution of the Algebraic Ricatti Equation and must be positive semi-definite. The use of quadratic form to generate these matrices assures that they are positive semi-definite.

The last variable was reserved for the sampling rate selection, thus $T = X(9)$.

4.3.3 Selecting The Starting Point For Optimization

Implementation of "constr.m" routine requires an estimate of a starting point (**X0**). In this section the starting point is selected based on derivations presented in paragraphs 4.1.1 and 4.1.2.

The poles contributed by the Kalman Filter and FSFB regulator were arbitrarily placed so that the three Kalman filter poles lie in the Butterworth pattern around 600rad/sec and the two regulator poles are located at $s_1, s_2 = -200 \pm j100$. Consistent with (4.11) the state weighting matrix that generates the desired pole location is

$$Q = \begin{bmatrix} 18400 & 0 \\ 0 & 8125.4 \end{bmatrix} \tag{4.33}$$

thus , in accordance with equation (4.31) , *X(1)* = 135.6 and *X(2)* = 90.14.

To obtain the Butterworth pattern with Ω = 600 rad/sec, according to equation (4.20), the covariance matrix *V* = 6.3183e15. Thus using equation 4.32 the coefficients *X(3)* through *X(7)* were set to zero and *X(8)* = 79.488e6.

The sampling rate variable *X(9)* was arbitrarily set to 1 millisecond.

4.3.4 Optimization Results

Due to high number of variables and poor variable scaling the numerical optimization routine exhibited numerous convergence problems. However, numerical problems were minimized by better variable scaling and controlling the maximum iteration step size. Matlab's "dstep.m" routine was used to simulate the closed-loop step responce. The optimal solution found by the optimization routine yielded a closed-loop system with step response overshoot of 52%. The corresponding Kalman Filter and FSFB gains were

$$K = \begin{bmatrix} K_d & K_v & K_f \end{bmatrix}^T = \begin{bmatrix} 0.69881 & 409.25 & 33175.0 \end{bmatrix}^T$$

$$G = \begin{bmatrix} g_d & g_v \end{bmatrix} = \begin{bmatrix} 7360.0 & 101.21 \end{bmatrix}$$

The sampling time selected by the optimization routine was 0.8 milliseconds.
The closed-loop poles corresponding to the above gain and sampling rate selections are located in the *z-plane* at

$$0.4683 \pm j0.3149$$
$$0.8727 \pm j0.0632$$
$$0.9048$$

which corresponds to the *s-plane* location

$$-715.09 \quad \pm j739.90$$
$$-166.92 \quad \pm j90.359$$
$$-125.29$$

The simulated step response of the optimized linear system is presented in figure 4.2. In linear simulation the peak is reached in 10 samples or 8 milliseconds.

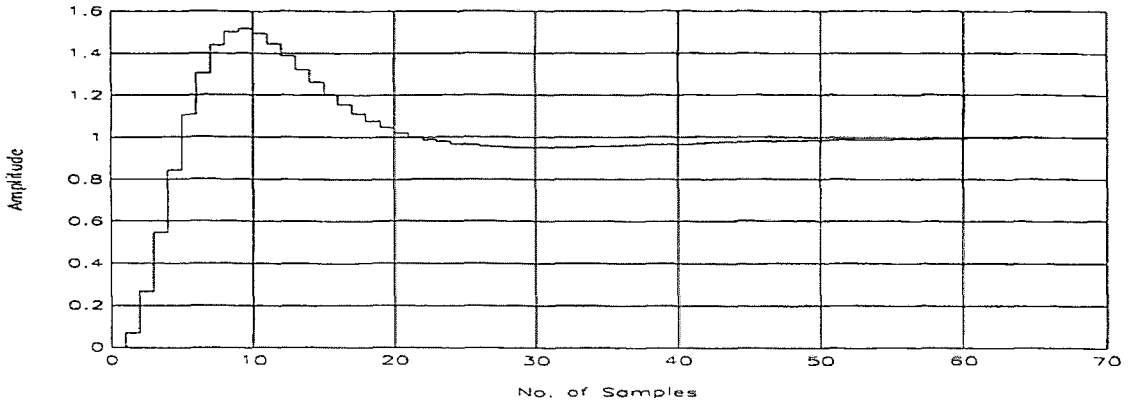

Figure 4.2 Linear Time Domain Simulation of Optimized System

The frequency response plot of the open-loop optimized system is shown in figure 4.3.

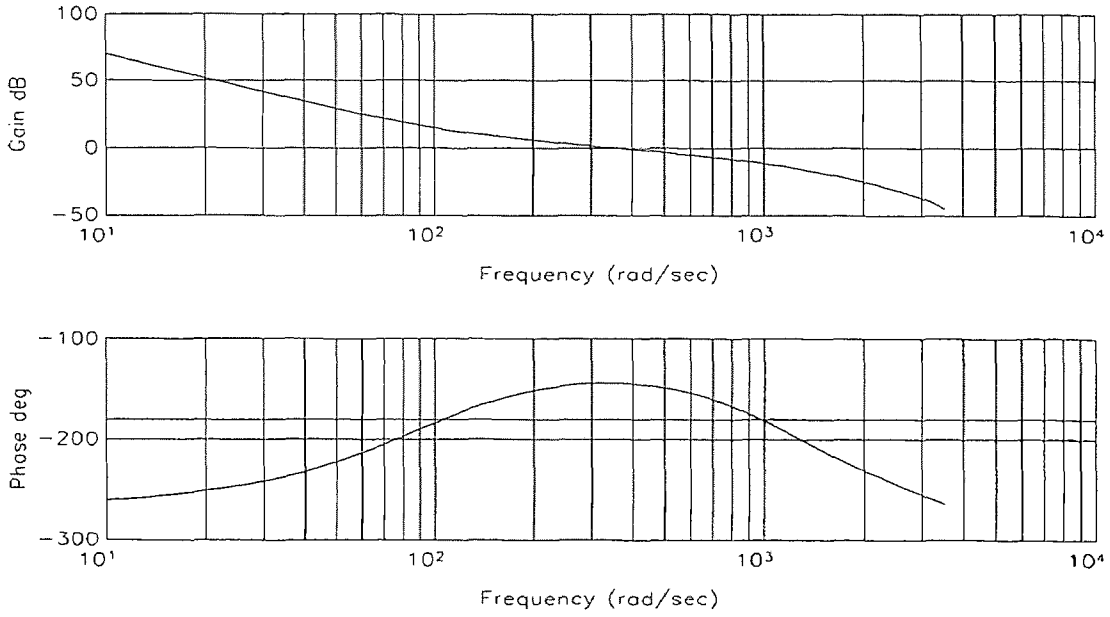

Figure 4.3 Small-Signal Frequency Response of the Optimized System

For the resultant system, the 0 dB crossover frequency $Wc = 370$ rad/sec, and Phase Margin is 36°. Note that since the system is open-loop unstable, there are two frequencies where the phase crosses 180°, thus there are two gain margins. The Gain Margins are 11 dB and -16dB.

The above results indicate that the optimized system is robust enough to absorb the actuator model uncertainties identified in Chapter 2.

CHAPTER 5

SIMULATION

In this section the nonlinear single-axis agonistic motion control system is simulated and compared to linear simulation results obtained in Chapter 4. The simulation is performed using VisSim® simulation software from Visual Solutions Inc.

5.1 Simulation Approach

The block diagram of the complete digitally regulated agonistic motion control system is shown in Figure 5.1.

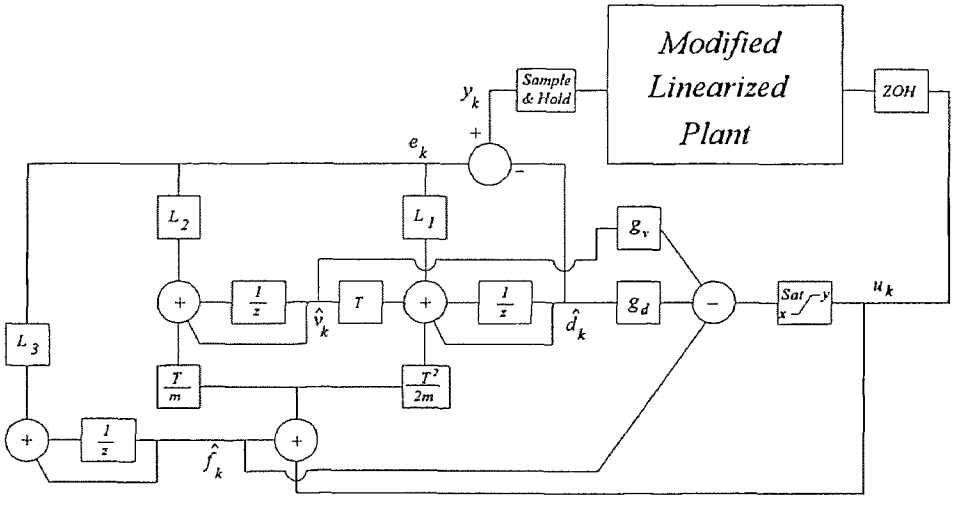

Figure 5.1 Block Diagram of Digital Control Law Simulation

The Kalman filter gains L_1 through L_3 and FSFB gains g_d and g_v used in the simulation are consistent with optimal gains selected in Section 4.3.4.

The control law was simulated using unit step delay terms (z^{-1}) with the Sample-and-Hold and Zero-Order-Hold functions included in the simulation. The sampling time was set to 0.8 milliseconds.

The saturation block was included to simulate the saturation properties of the solenoid as predicted by the real-time linearization algorithm. The variable saturation limits were calculated within simulation as a function of the actual displacement. The saturation forces were calculated per defining equation (2.7) for maximum current supplied by the Power Amplifier ($i = 4A$). The positive saturation limit is the maximum force that the left solenoid can produce at a given displacement and the negative limit is the maximum force for the right solenoid.

5.1.1 Modified Linearized Plant Simulation

Additional modifications were made to improve simulation accuracy of the linearized plant. The block diagram for the modified linearized plant is shown in Figure 5.2. The "*Saturation Simulation*" block was used to describe the core saturation effects at high input currents and low displacements. The need for this block is evident from the curve-fitting results presented in table 2.3 which shows that the force estimate obtained from the defining equation (2.7) is higher than actual for forces in excess of approximately 35 Newtons. This is a core saturation phenomenon where input current increase produces reduced increase in flux and in the generated force. This nonlinear effect was

approximated by the function shown in the "*Saturation Simulation*" block in figure 5.2. Its transfer characteristics are shown in figure 5.3.

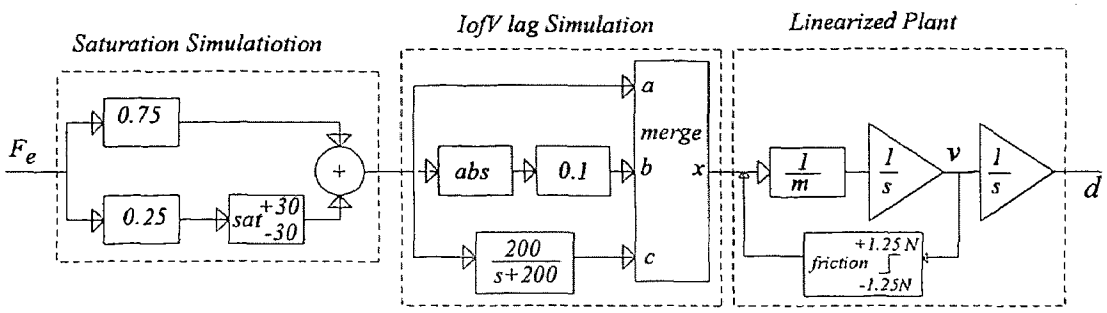

Figure 5.2 Block Diagram Modified Linearized Plant

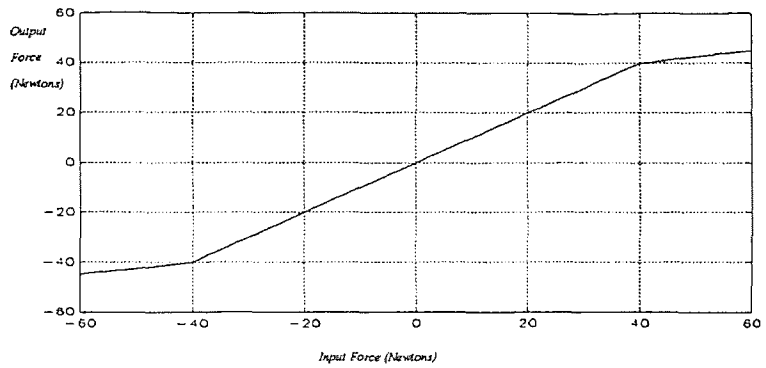

Figure 5.3 Transfer Characteristics of "Saturation Simulation" Block

The characteristics of the Voltage Controlled Current Source are simulated in the "*I of V Simulation*" block. The Voltage Controlled Current Source was designed to supply a current output proportional to the input control signal. Under small-signal excitation this

approach masked the pole introduced by the solenoid inductance (See Chapter 6). However, under large-signal excitation, the inductance effects are noticeable because the excitation voltage of the Voltage Controlled Current Source is finite, thus a low-pass transfer characteristics are introduced. In simulation diagram the "merge" function in the *"I or V Simulation"* block is used to combine the large- signal dynamics of the Currents Source with the small-signal characteristics. The "merge" block function is defined

$$x = \begin{cases} a & for \quad b \le 1 \\ c & for \quad b > 1 \end{cases}$$

thus the low-pass dynamics are introduced within the simulation when the control force magnitude is above 10 Newtons and bypassed for lower-level control signals.

The *"Linearized Plant"* portion of the modified linearized plant diagram is the approximation of the linear portion of the second order motion control plant.

5.2 Simulation Results

The simulation of the non-linear system has revealed some deviation from the results predicted by linear simulation. Experimental simulation parameter variation revealed that the major contributor to deviation was the actuator saturation. Friction effects were negligible.

Figure 5.4 shows the simulated response to 0.01 meter step reference change for the digitally controlled nonlinear agonistic system with linear and with saturable actuator. Position error is shown. The payload initially located at 0.0034 meters absolute displacement is programmed to move to 0.013 meters position.

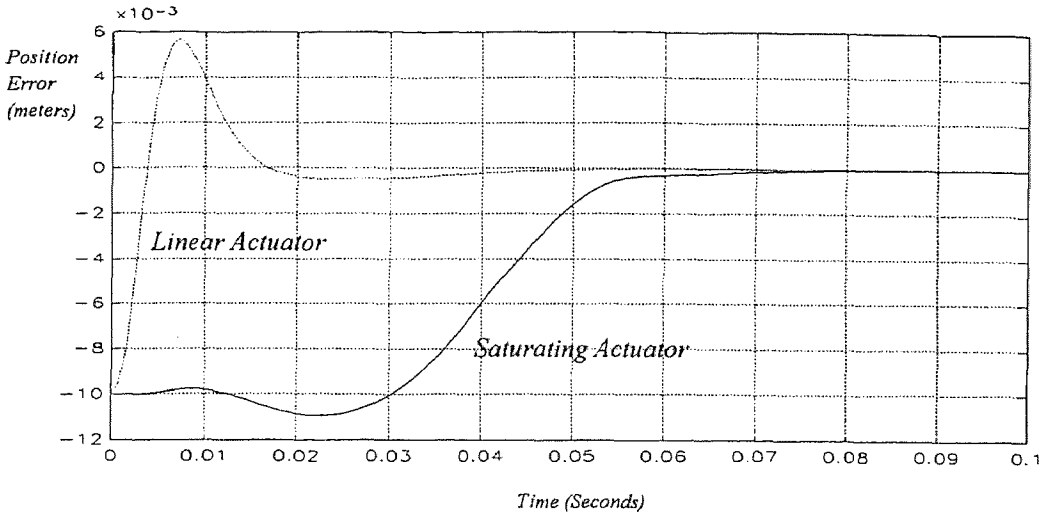

Figure 5.4 Simulated Step Response with 0.01m Step Reference Command

The system response with linear actuator is approximately 8 milliseconds which is consistent with linear simulation results shown in figure 4.2, however, in presence of the actuator saturation the payload position reaches 90% of programming in almost 50

milliseconds. Furthermore, at approximately 20 milliseconds the payload appears to move in the wrong direction. This phenomenon is related to the modeling uncertainty and is caused by the saturation force unbalance at selected displacement. Namely, at the 0.0034m initial starting point, the left solenoid is capable of generating a force of 20 Newtons while the right solenoid can produce up to 70 Newtons, thus while Kalman Filter is converging, the movement to the right is observed. The force outputs for the linear and saturable actuator plants are compared in Figure 5.5.

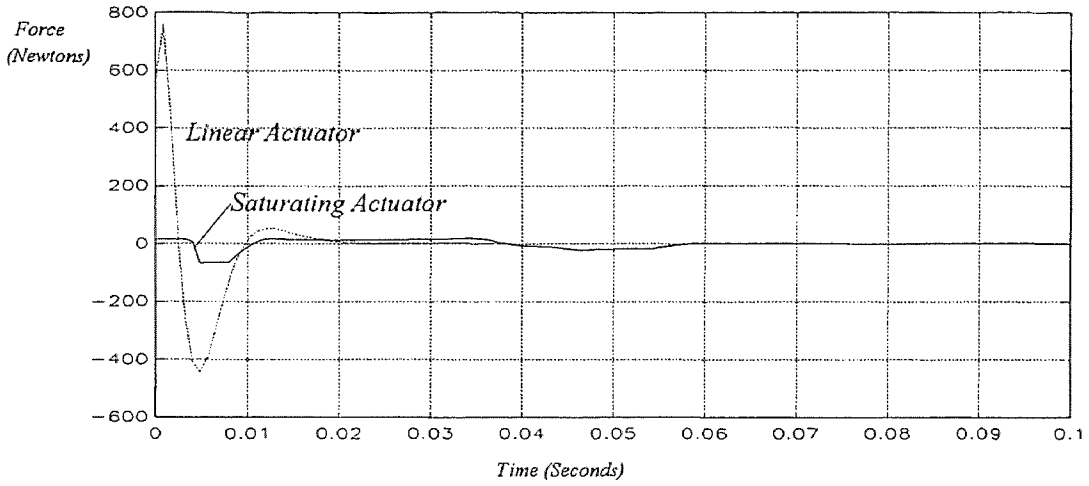

Figure 5.5 Force Output with 0.01m Step Reference Command

As expected, the saturation effects are milder at lower step reference programming levels. Figure 5.6 shows the 0.001 meter simulated step reference response. The initial load position is 0.0084 meters absolute displacement. The rise time for 0.001meter programming command is reduced to 30 milliseconds. The force outputs for the linear

and saturable actuation models for 0.001 meter step reference condition are compared in Figure 5.7.

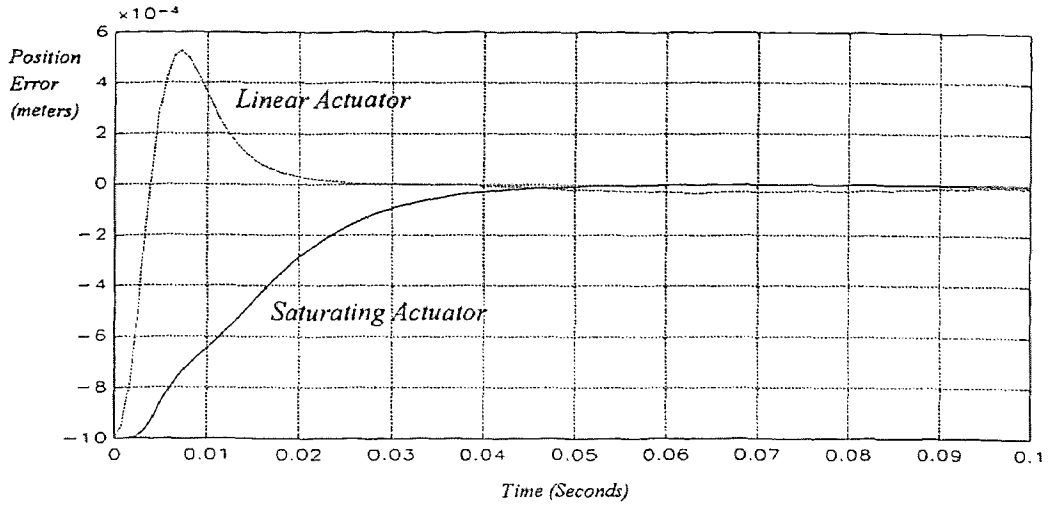

Figure 5.6 Simulated Step Response with 0.001m Step Reference Command

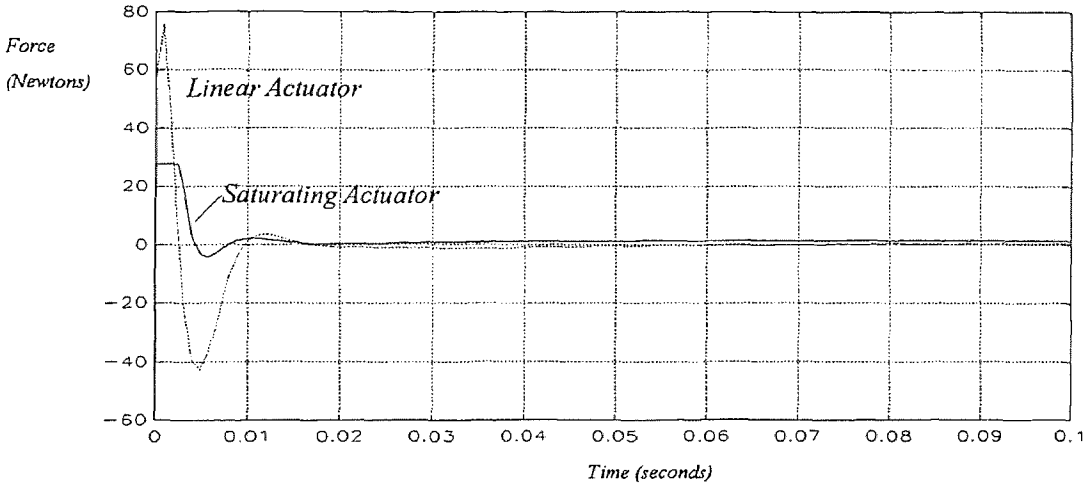

Figure 5.7 Force Output with 0.001m Step Reference Command

5.3 Reference Input Location

The step reference response of the single-axis motion control agonistic system may be improved by alternate selection of a point where the reference signal is input.

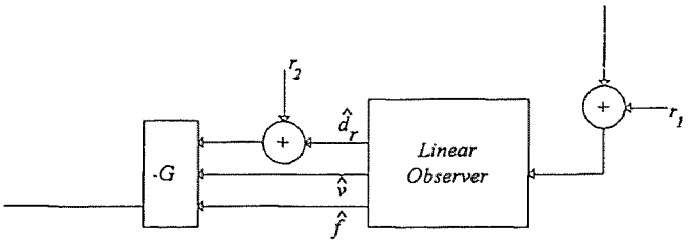

Figure 5.8 Alternate Reference Input Location

This concept is demonstrated in Figure 5.8. For previous simulations the reference was subtracted from the actual feedback signal (shown as r_1) thus, given a step reference change, Kalman Filter had to estimate the reference before the control was generated. In presence of actuator saturation, the above sequence caused a 20 to 30 millisecond delay. However, subtracting the reference from the position estimate $\hat{d}$ (shown as r_2) the Kalman Filter dynamics are virtually "bypassed" thus improving the overall programming step response.

The simulation results with two alternate reference locations are compared in Figure 5.9 where *Curve A* is the step response with reference subtracted from $\hat{d}$ (r_2) and *Curve B* is the response to step reference subtracted from the feedback (r_1).

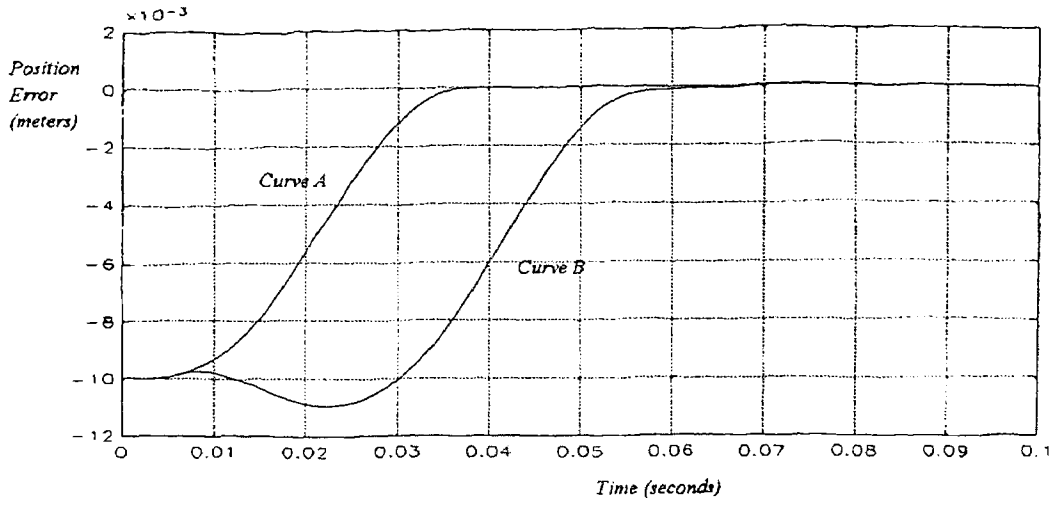

Figure 5.9 Alternate Reference Input Simulation

Thus in this particular application, faster step reference response is achieved when the reference is subtracted from the position estimate $\hat{d}$ (r_2) rather than the actual feedback. However, the reference input location has no effect on the systems response to output disturbance, thus, the optimization performed in section 4.3 where the reference is subtracted from the feedback is justifiable because this simulation describes effects of load disturbance.

CHAPTER 6

IMPLEMENTATION

6.1 Hardware

The experimental setup presented in figures 6.1. and 6.2. represents the motion control system described in Chapter 1 of this document.

The prototype was constructed on a 0.5" thick aluminum plate that measures 12" by 20". At the heart of the motion control system is the agonistic control plant constructed of two opposing solenoid electromagnets. The spacing between solenoids is selected to allow a 0.8" (0.02032 m) payload travel.

The *Solenoid Magnets* selected for this design are D-Frame Intermittent Duty devices Part No.53719-87 manufactured by Deltrol Controls. They are capable of 1.0" travel and can develop forces in excess of 40 lb. at small plunger displacements.

The 13 ounces (0.368 Kg mass) *payload* is secured directly to the solenoid plungers. It should be noted that 13 oz. weight includes the weights of the solenoid plungers that weigh 3 oz. each. This rigid rod construction may seem as a departure from the agonistic control notion, however, since solenoid generates force only in the direction of decreasing displacement, the rigid rod construction by no means violates the concept of agonistic control, yet greatly simplifies the mechanical construction by providing convenient means of direct position sensing.

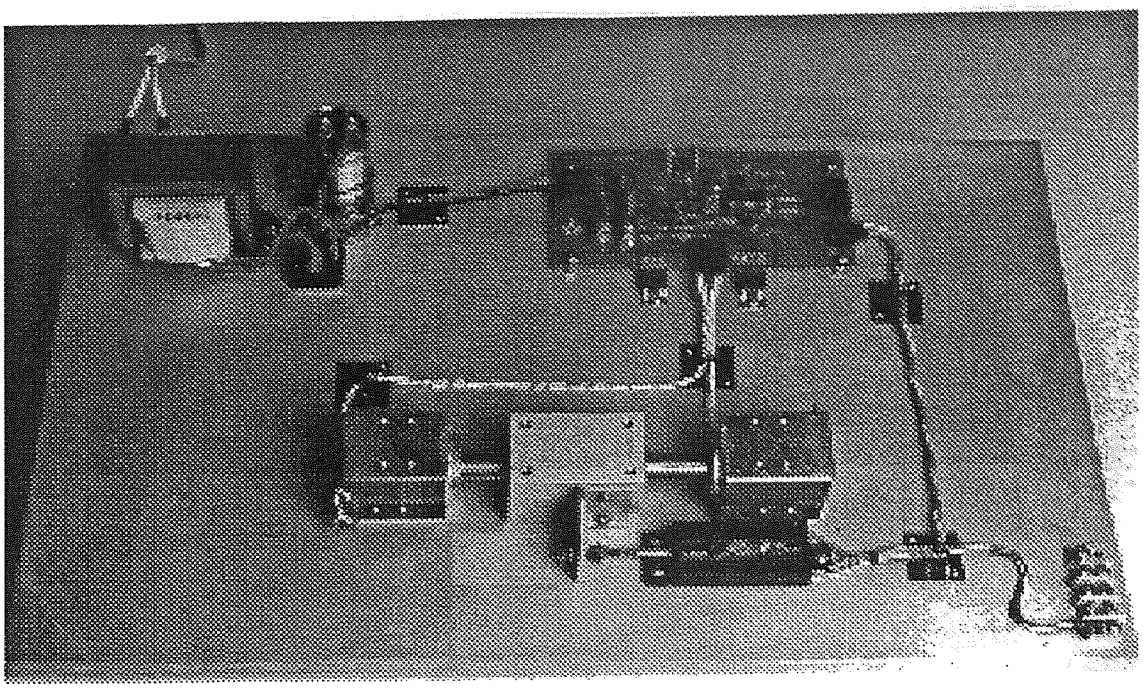

Figure 6.1 Construction of 2-Axis Agonistic Motion Control System

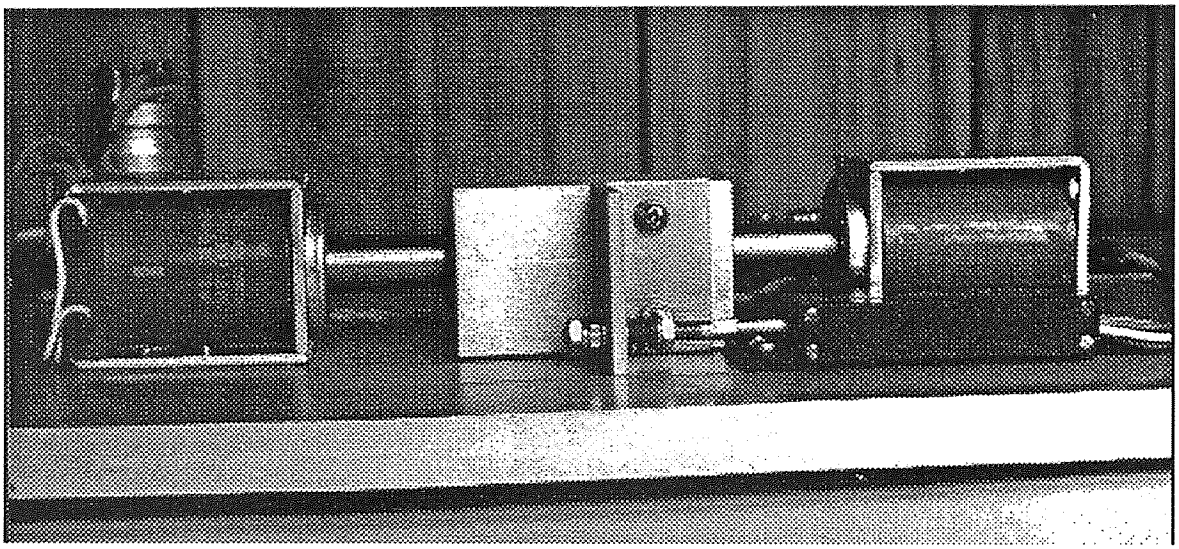

Figure 6.2 Close-up of 2-Axis Agonistic Plant

A *Voltage Controlled Current Source* (I of V) was used to energize the solenoids. The Voltage Controlled Current Source selection was based on the fact that the force generated by the solenoid, is a function of input current. When driven with a voltage source system dynamics are augmented with a pole at location $\omega = L/R$ where R is the solenoid coil resistance and L is the coil inductance. Furthermore the coil inductance is not constant and varies nonlinearly with plunger displacement. While it is still possible to account for these secondary dynamic effects in the control algorithm, the additional dynamics needlessly complicate the control algorithm and may result in slower sampling rate and inferior system response time.

The position feedback is accomplished by a *linear potentiometer* whose plunger is fastened to the payload. The selected potentiometer is a plastic film element device manufactured by Markite (type 2986). Its electrical travel is 1.0" and mechanical travel is 1.3" . The plastic film construction provides virtually infinite resolution. The friction or the *actuation force* for the chosen potentiometer is specified at 6oz. (1.67 N) maximum, the actual measurements indicate that the actuation force for the given device is approximately 4.5 oz. (1.25 N).

Due to minute misalignments in lines of action of the two solenoids and potentiometer plunger, an inflexible connection between the potentiometer plunger and the payload resulted in binding. This situation was remedied by adding a stiff compression spring at the potentiometer and payload tie point as shown in figure 6.3. The spring allows minimal centroidal (joystick)rotation about the fixed point thus reducing binding effects without noticeable effect on displacement sensing.

A precision *Reference and Scaling Amplifier* were designed to interface with the potentiometer. The 10.00 Volt reference was generated by an Analog Devices Precision reference I.C. AD584ST. The scaling amplifier constructed with a precision quad Op-Amp I.C. manufactured by Linear Technology (P/N LT1014J). The gain of the scaling

amplifier was set so that the 0.0 to 10.0 Volt output corresponds to extreme Left to extreme Right payload positions respectively.

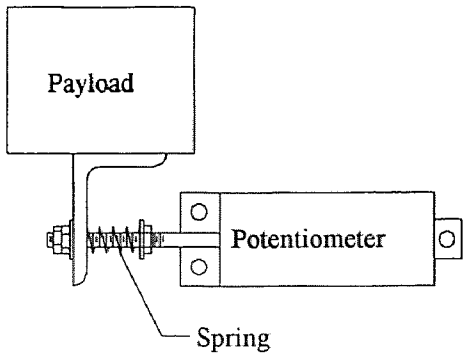

Figure 6.3 Method for Reducing Binding

In order to limit the exposure of Analog to Digital converters to the frequencies that are higher than the sampling rate an anti-aliasing *Low-Pass Filter* is used. For this experiment the single stage RC filter with 500 Hz break frequency was selected.

The schematics and the parts lists for the above are listed in Appendix A of this document.

The control algorithm for the single-axis agonistic control was implemented on an IBM compatible 80386 25 MHz computer equipped with an ADA2210 *Advanced Data Acquisition and Control board.* The ADA2210 Advanced Data Acquisition and Control board has up to 8 differential or 16 single-ended scaleable analog inputs with 12 bit resolution. Only one single-ended input scaled for unidirectional 10 Volt operation was used in this project. The two Digital-to-Analog outputs were used to control the solenoid currents. They were scaled identically to the input. The internal 8254 Timer/Counter was set for 0.8 millisecond sampling.

6.2 Software

The real-time control algorithm was written and implemented using Borland C++ version 3.0 compiler. The complete source code is listed in Appendix B.

The control algorithm was granted complete control of computer's resources by keeping all interrupts normally masked and enabled periodically only to acquire the keyboard status. This technique assured better control over the sampling timing which is important in applications where the sampling rate must be maximized for best performance. In Interrupt Service Routine (ISR) applications the priority with which the control interrupt routine is serviced is at the mercy of the hardware architecture. Namely, an interrupt routine of higher priority may be called during the execution of the control routine, or an interrupt of the same priority may be called just before the timer signal. Either condition will interfere with proper timing and execution of the real-time control routine.

The flow chart describing the logical flow of the program is shown in figure 6.4, the program source code is listed in Appendix B of this document, and the control law application summary is given in section 6.2.1.

The execution time for this program on the 80386A 25MHz computer was measured with an oscilloscope by monitoring one digital output of the Data Acquisition Board that was set "high" at the beginning of the timing cycle and was reset after the control is output. During normal operation the program execution time was measured at 0.35 milliseconds. As seen from the flow chart, additional computations are required in the event of actuator saturation. The computational delay in that instance was measured less than 0.8 milliseconds. These results were used in the parameter optimization section of this document.

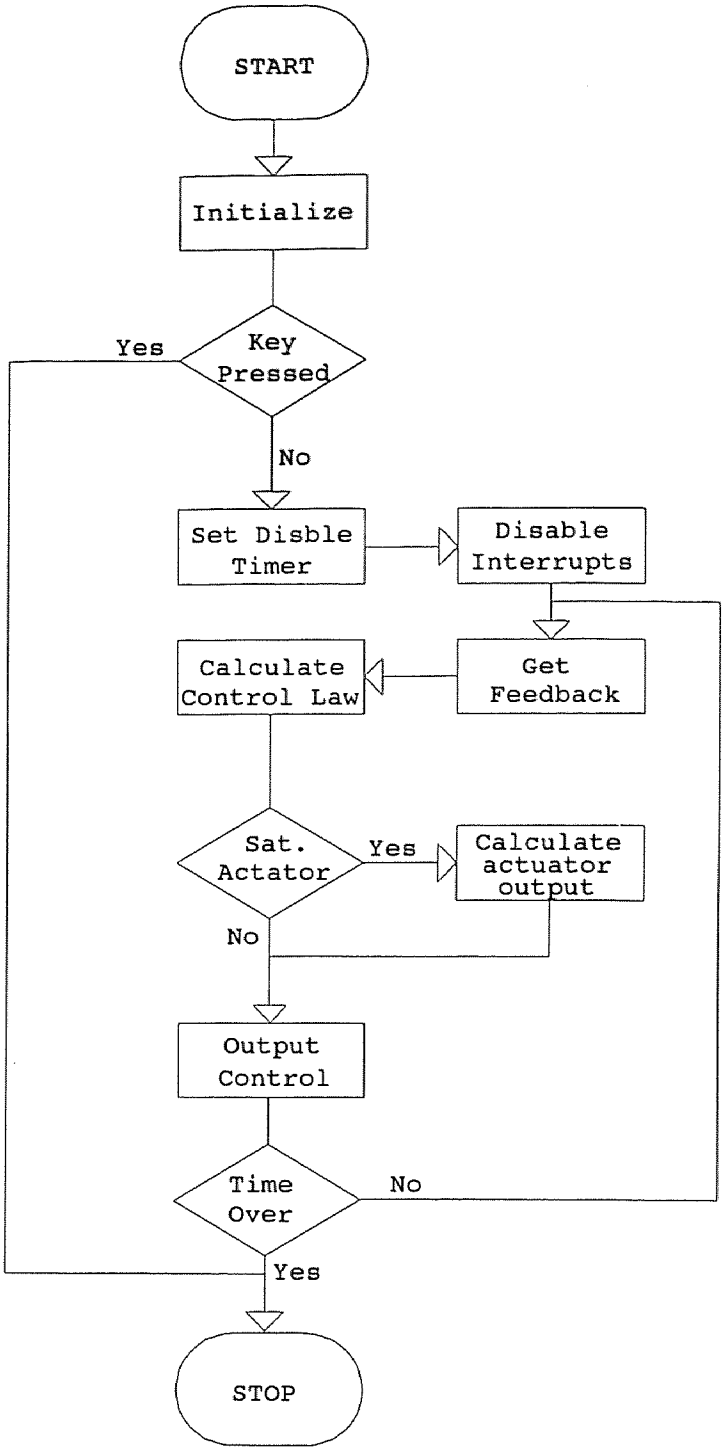

Figure 6.4 Flow Chart for Agonistic Plant Control Computer Algorithm

The program allocates all processing power of the computer to the control algorithm and acquires the keyboard status every 3 seconds. With no commands from the keyboard the preprogrammed position reference is toggled each time the keyboard status is checked. The control execution is terminated at the end of the 3 second period if a key was pressed.

As an added feature the means of recording the performance data were provided. The actual feedback and estimated output force were collected in this particular application. The variables of interest are stored in the array at the completion of each computational cycle. The contents of the array are copied into the text file "data.out" before exiting the control program.

6.2.1 Control Law Application Summary

In this section the procedures developed in preceding sections are summarized to aid in understanding of the control law implementation and to follow the program source code.

1. All variables are initialized prior to entering the main control loop and the Kalman filter auxiliary gains are calculated per equation 4.29.

$$\begin{bmatrix} L_1 \\ L_2 \\ L_3 \end{bmatrix} = \begin{bmatrix} K_d + K_v T + K_f \dfrac{T^2}{2m} \\ K_v + K_f \dfrac{T}{m} \\ K_f \end{bmatrix}$$

2. In the main control loop the feedback is first obtained.

3. The Kalman filter dynamics are calculated per equation 4.28

$$\hat{d}_{k+1} = \hat{d}_k + T\hat{v}_k + \frac{T^2}{2m}\left(\hat{f}_k + F_k\right) + L_1\left(y_k - \hat{d}_k\right)$$

$$\hat{v}_{k+1} = \hat{v}_k + \frac{T}{m}\left(\hat{f}_k + F_k\right) + L_2\left(y_k - \hat{d}_k\right)$$

$$\hat{f}_{k+1} = \hat{f}_k + L_3\left(y_k - \hat{d}_k\right)$$

4. The linear control output is calculated using equation 4.8

$$F = -g_d d - g_v v - f$$

5. The forces in left and right solenoids are determined from equation 3.3

$$F_L = \begin{cases} F + Tension & for \;\; F > 0 \\ Tension & for \;\; F \le 0 \end{cases} \quad \text{and} \quad F_R = \begin{cases} -F + Tension & for \;\; F < 0 \\ Tension & for \;\; F \ge 0 \end{cases}$$

6. The corresponding current programming signals are calculated from equation 2.6

$$i_L = \sqrt{(F_L{}^2 + 45.669F_L)\cdot(47.003d_L{}^2 + 0.4312d_L + 0.000204)}$$

$$i_R = \sqrt{(F_R{}^2 + 45.669F_R)\cdot(47.003d_R{}^2 + 0.4312d_R + 0.000204)}$$

7. If one of the calculated currents exceeds the preset limit, its amplitude is constrained and the saturation force produced by the respective solenoid is recalculated using equation 2.7

$$F_x = \sqrt{521.423 + \frac{i_x^{\,2}}{47.003 d_x^{\,2} + 0.4312 d_x + 0.000204}} \; - \; \sqrt{521.423}$$

The estimate of the actual force acting on the payload is obtained from

$$F = F_L - F_R$$

and is used for the next calculation cycle.

6.2.2 Additional "Lead" Compensation

The apriory recursive observer formulation assumes that the control is output just prior to the start of a new computation cycle, however, outputting the control t_l seconds prior the start of a new cycle will have an effect of a phase lead. This phenomenon was used in the control law to help counterbalance the phase lag caused by the magnetic hysteresis of the solenoids. Namely , with the sampling rate set at 0.8 milliseconds and computation time of 0.35 milliseconds it is possible to output the control 0.45 milliseconds before it is expected. At 370 rad/sec 0dB crossover frequency the 0.45 millisecond lead translates in a 10° phase lead thus helping to counterbalance a typical 20° phase lag inherent in the magnetic structure of the solenoid (see paragraph 2.2.3).

CHAPTER 7

PERFORMANCE TEST RESULTS

In this chapter the closed-loop system performance is evaluated by examining the system response to a step disturbance and a step reference. The measured results are summarized and compared to simulation predictions. The *position error* and the *net force* information is collected using the recording feature of the real-time control program presented in Appendix B. The actual feedback signal was used to identify the payload position. The variations due to the potentiometer nonlinearity and limited repeatability were ignored.

System step response was evaluated for both reference input locations as defined in paragraph 5.3. The system response to the output disturbance was determined with reference subtracted from the actual feedback while step-reference response was evaluated with reference subtracted from the position estimate.

7.1 Step Disturbance Response

The tests in this section evaluate the closed-loop system response assuming an instantaneous change in displacement due to an external excitation or a "cold start" condition. This simulation is accomplished by varying the reference that in turn is subtracted directly from the actual feedback.

The measured response to a 0.01 meter step feedback change is compared to simulation results in figures 7.1 and 7.2. For the purposes of this test, the payload initially located at 3.4 millimeters absolute displacement is programmed to move to 13.4 millimeter location. The position error response is shown in figure 7.1 and the forces predicted by the simulation and the control program's linearization algorithm are compared in figure 7.2.

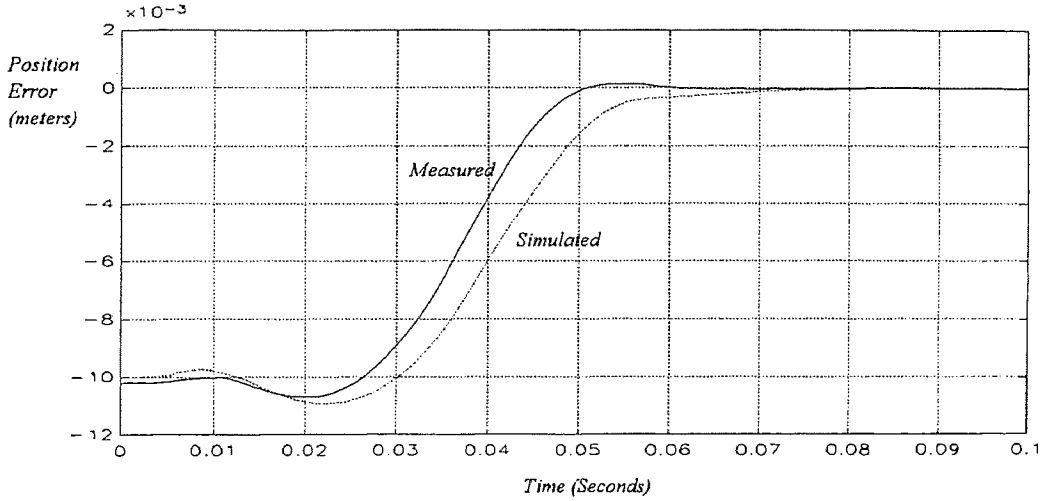

Figure 7.1 Position Error Response to 0.01 m Step Disturbance

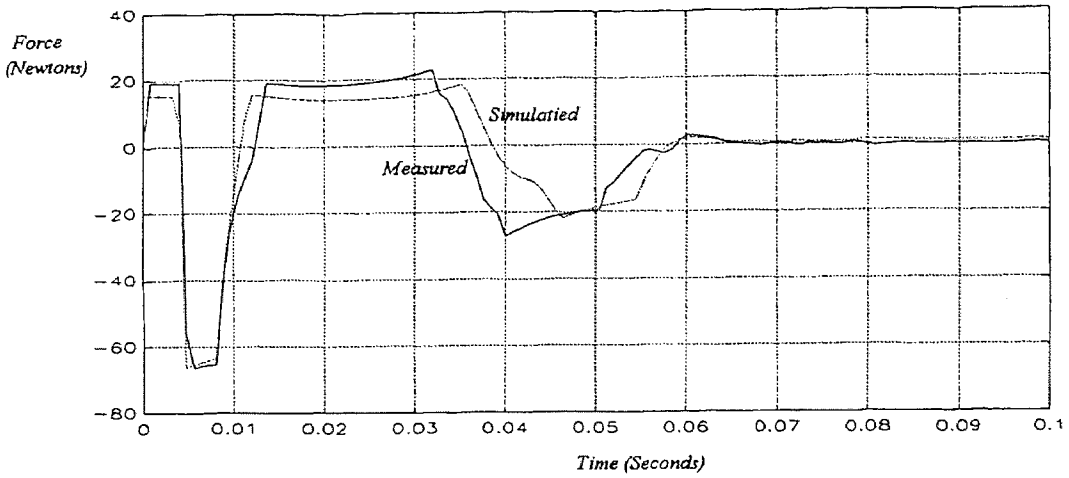

Figure 7.2 Force Response to 0.01 m Step Disturbance

The general shape of the measured response is consistent with the predicted results though the measured response is approximately 5 milliseconds faster than the simulation. The discrepancy between measured and simulated results is present because simplified model of friction and actuator saturation were used in the simulation.

The behavior of the compensated system under low-level disturbance perturbations was evaluated by observing the system behavior under 0.001 meter reference change. The position error and the force estimates for the 0.001 meter reference change are shown in figures 7.3 and 7.4 respectively. The initial absolute payload position for measurement and simulation was 8.0 millimeters.

As expected, the response time to lower signal excitation is faster due to milder actuator saturation effects. The response time to 0.001 meter disturbance step is approximately 35 milliseconds as opposed to 47 milliseconds response to 0.01 meter disturbance step.

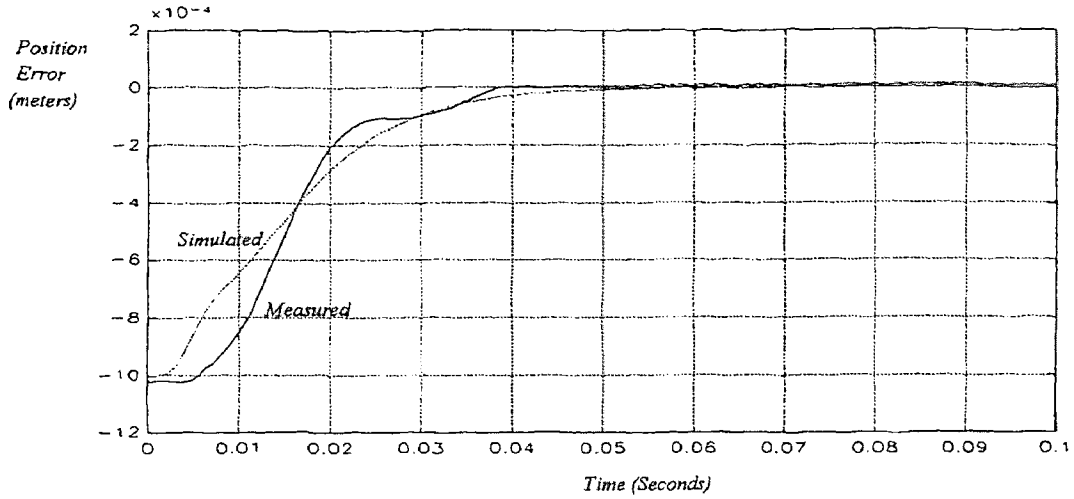

Figure 7.3 Position Error Response to 0.001 m Step Disturbance

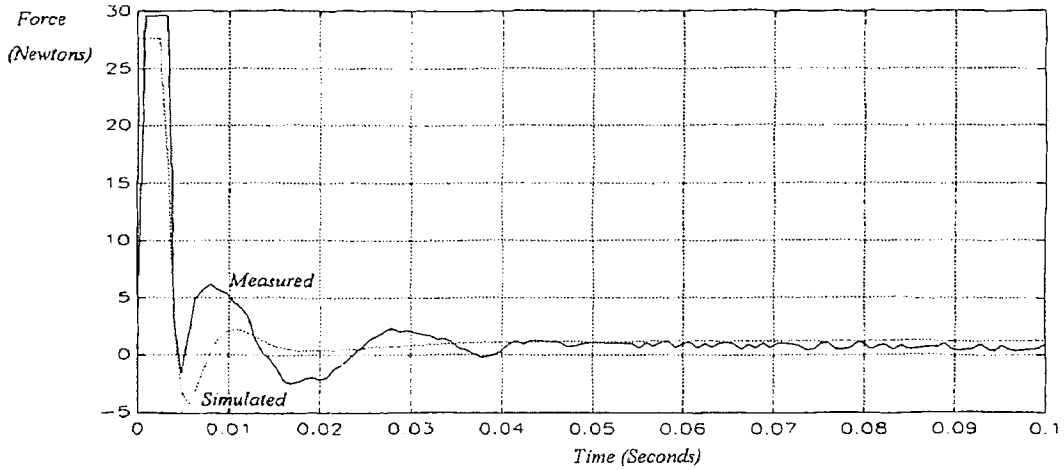

Figure 7.4 Force Response to 0.001 m Step Disturbance

A difference between the measured and simulated position error results is noticeable in the curvature of the response. While the overall measured rise time is consistent with predicted results, the shape of the measured response is initially slower than predicted. It is speculated that this phenomenon is contributed by the unmodeled "sticktion" element and approximate modeling of the delay caused by the large-signal response of the actuator.

7.2 Step Reference Response

In this section the test and simulation results for the system where the reference is subtracted from the estimated position are presented. As shown in paragraph 5.3 this control method is expected to improve the step reference response of the system.

The 0.01 meter step reference response measurements and simulations are shown in figures 7.5 and 7.6. The position error response is shown in figure 7.5 and the forces predicted by the simulation are compared to the forces predicted by the control program's linearization algorithm in figure 7.6. Similarly to the experiments presented in section 7.1, the payload initially located at 3.4 millimeter absolute displacement is programmed to move to 13.4 millimeter location. The improved reference tracking ability of the proposed reference location is evident by comparing the results of figure 7.1 to figure 7.5. The payload reaches 90% of the programmed travel in less than 28 milliseconds while the rise time for the same conditions with reference introduced at the feedback (figure 7.1) is 48 milliseconds.

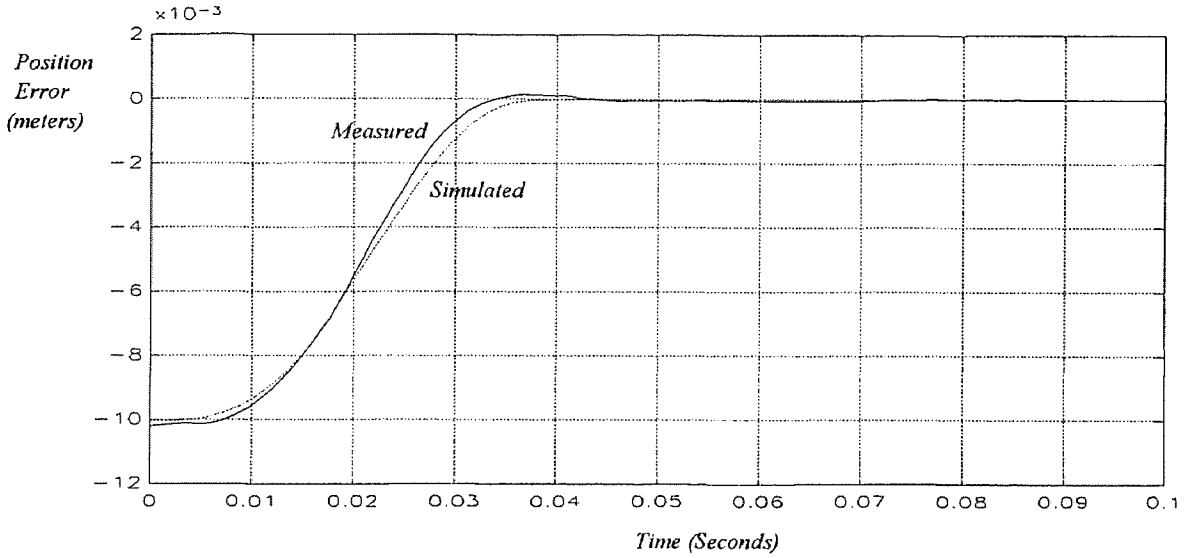

Figure 7.5 Position Error Response to 0.01 m Step Reference

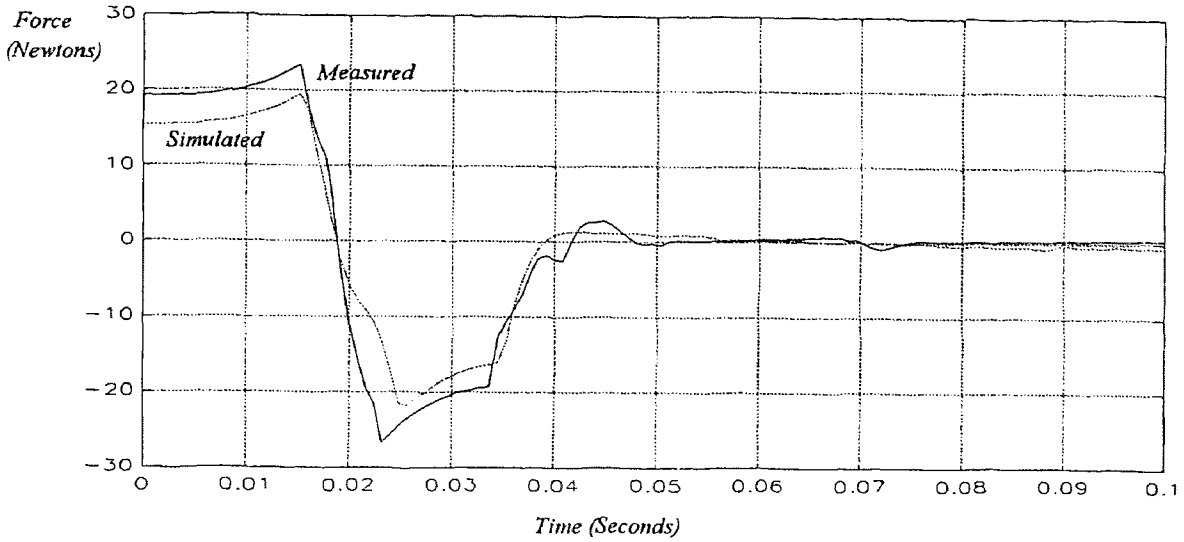

Figure 7.6 Force Response to 0.01 m Step Reference

The differences between the simulation prediction and the measured response in figure 7.5 in contrast with figure 7.1 where 5 millisecond rise time discrepancy was observed are negligible. The improved simulation accuracy is explained by the fact that the above controller configuration generates a softer control output with less severe actuator saturation thus the errors due to approximate nature of the large-signal actuator model are minimized. The position error response for the 0.001 meter reference change with initial absolute payload position at 8.0 millimeters is shown in figure 7.7.

Similarly to results shown in figure 7.3 the shape of the measured low-level signal response differs from the simulation. The measured rise time to the 0.001 meter reference step is 30 milliseconds as compared to predicted 25 milliseconds. While the overall measured rise time is comparable to predicted results, the shape of the predicted response differs from measured trajectory due to approximations in actuator and friction modeling.

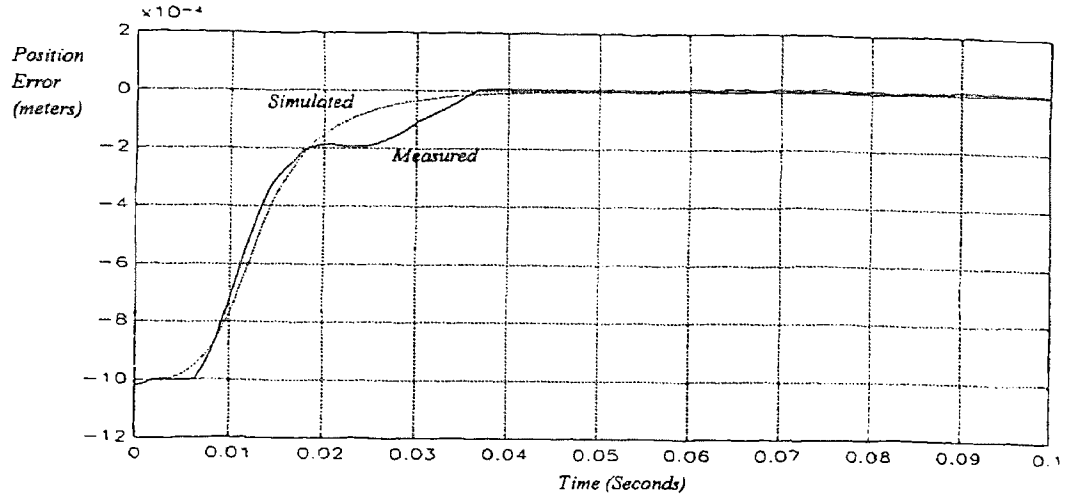

Figure 7.7 Position Error Response to 0.001 m Step Reference

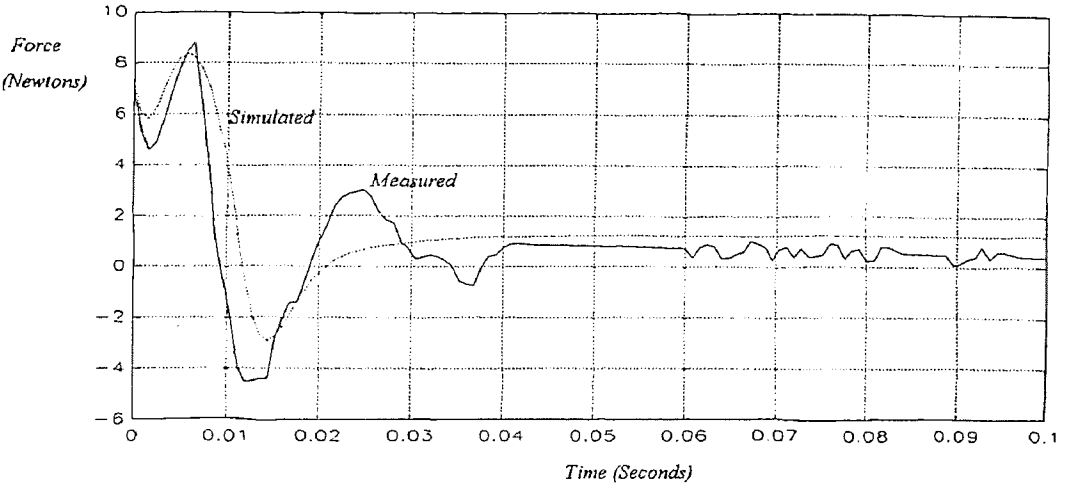

Figure 7.8 Force Response to 0.001 m Step Reference

It should be noted that the differences in the system response time for low-level reference perturbations are less dependent on location of the reference summation signal as evident from comparing figures 7.3 and 7.7. While alternate reference summation location has improved the step response time to 0.01 meter reference step by 20 milliseconds (figures 7.1 and 7.5) , the improvement is much less noticeable under the 0.001 meter excitation.

7.3 Steady-State Performance

The controller designed for this project was designed to provide integral action to assure minimal steady-state error. In linear system the controller with integral action assures that the steady-state error will converge to zero with time, in quantized systems, however, the error is finite. The quantized error in this project is governed by the resolution of the 12Bit Analog-to-Digital Converter to 1/4095 of full scale which corresponds to 4.4 micron displacement error. With selected data acquisition hardware the controller with integral action is expected to maintain the payload position error in a window with 4.4 micron amplitude.

The integral action of the controller was verified by examining the position error on extended time scale. The position error for the 0.01 step reference response over the time span from 0.1 to 0.4 seconds is shown in figure 7.9 and repeated over the time span from 0.08 to 2 seconds in figure 7.10.

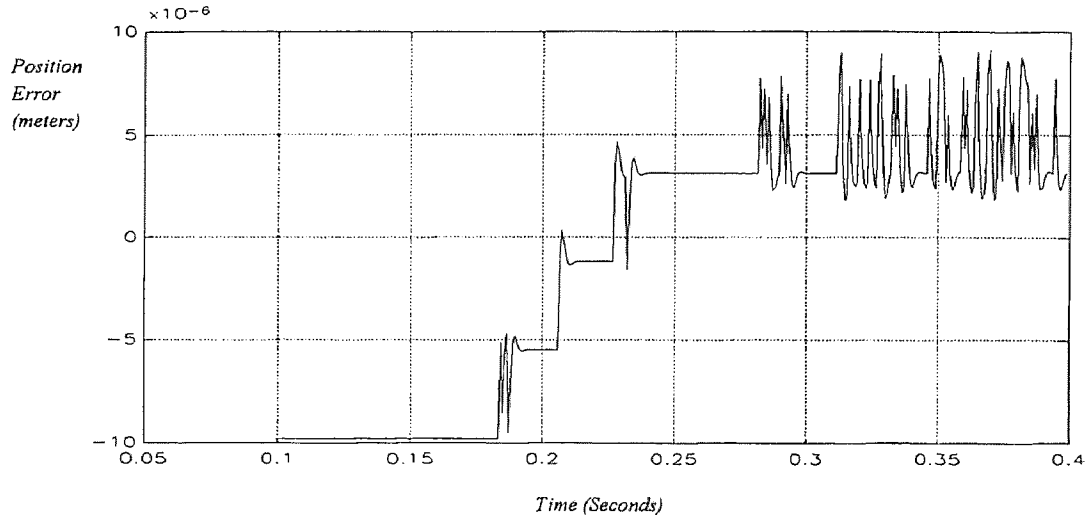

Figure 7.9 Position Error Over 0.1 to 0.4 Seconds

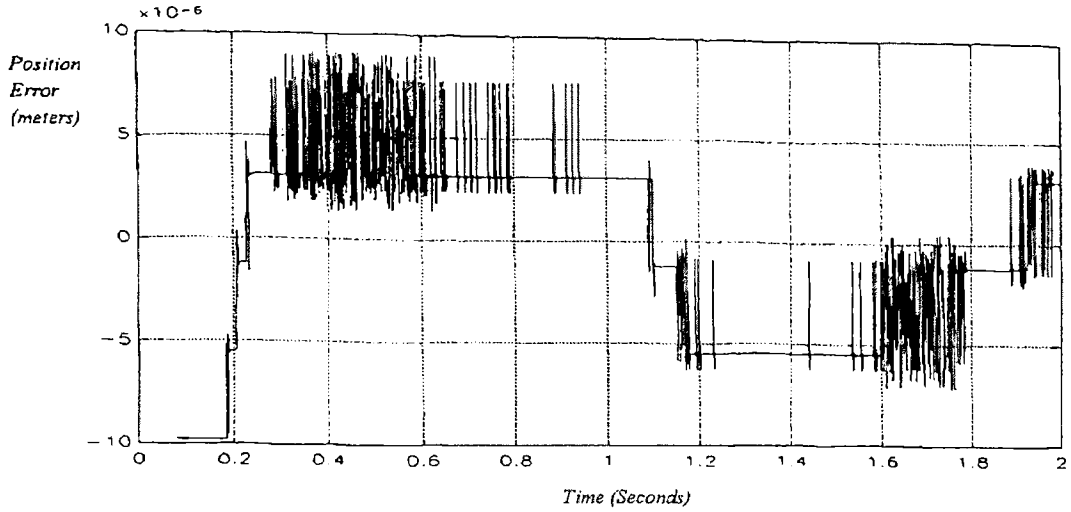

Figure 7.10 Position Error on Expanded Time Scale

The position error reaches the least significant bit accuracy in less than 200 milliseconds. Upon reaching the quantization limits the measurement alternates in the LSB resolution window.

CHAPTER 8

CONCLUSIONS AND OBSERVATIONS

The research presented herein establishes the feasibility of a single-axis agonistic motion control system actuated by two solenoid electromagnets where the workpiece is pulled to desired location by tendons that remain under tension.

The feedback linearization method was used to control the nonlinear plant. The selected control method resulted in a simple control law because the individual solenoid forces were known, thus the tendon tension was controlled algebraically with no augmented dynamics (paragraph 3.1).

The actuator model was developed in chapter 2 from basic dependencies and measured data . The empirical data was used to establish a static time-invariant memoryless dependency known as the defining equation. The high frequency actuator parameters were identified to assure robustness margin sufficiency.

A linear controller comprised of a Linear Quadratic Regulator and a Kalman filter for the linearized plant was designed in chapter 4. The Controller design used the direct discrete-time approach. The optimal gain coefficients were selected by numerical means to enhance desired performance parameters for the linearized system. The design optimization resulted in a open-loop system with 0 dB crossover frequency at 370 Rad/Sec, minimum phase margin 11dB, and phase margin of 36°.

The nonlinear single-axis agonistic motion control system was simulated and compared to linear simulation. Effects of actuator saturation and friction were examined. Alternate reference input locations were investigated and results were compared in chapter 5.

The prototype system construction was described in chapter 6. The single-axis construction prototype allowed some simplifications such as direct payload position sensing and rigid rod construction that are not possible in multi-dimensional agonistic motion control application. The control algorithm was translated in the computer code and implemented on an IBM compatible 80386 computer equipped with ADA2210 Advanced Data Acquisition and Control board.

The time domain design performance parameters were verified on a working prototype. The closed-loop system is capable of positioning the 0.75 pound payload over the .5" travel in approximately 30 milliseconds. The response was faster for lower step reference excitation levels.

The major system performance limiting factors were the computer speed and measurement resolution. The control routine execution time was measured at 0.8 milliseconds thus limiting the maximum sampling rate while the positioning accuracy was limited by the 12 Bit A-to-D converter resolution to 4.4 microns. However, these deficiencies may be readily addressed in future designs with faster hardware and more advanced position sensor selection.

This thesis focused on the development of a single-axis agonistic motion control system, however the broader application of developed theory and procedures described herein may be used in more advanced applications. Superior accuracy, fast response

speed, and low cost prove the agonistic motion control approach a strong challenger in the agile manufacturing environment. That cost and complexity can be reduced in such applications and environments warrants further investigation and evolutionary expansion into development of multi-axis agonistic motion control systems.

APPENDIX A

CUSTOM CIRCUITS DEFINITION

The information presented in this appendix describes the electronic interface circuitry that was designed specifically for this project and is intended to supplement the data presented in the hardware description section 6.1.

The aim of this section is to provide a description of the electronic interface circuitry that was designed specifically for this project. The information presented herein is intended to supplement the data presented in the hardware description section 6.1.

The special interface circuitry designed for this project consists of the *Power Supply*, two *Voltage Controlled Current Sources*, *Precision Reference*, and a *Scaling Amplifier*. The circuitry was combined on one Printed Circuit Board (PCB). The schematic of the combined circuit and the PCB layout are shown in figures A.1 and A.2 respectively. The detailed parts listing is given in Table A.1.

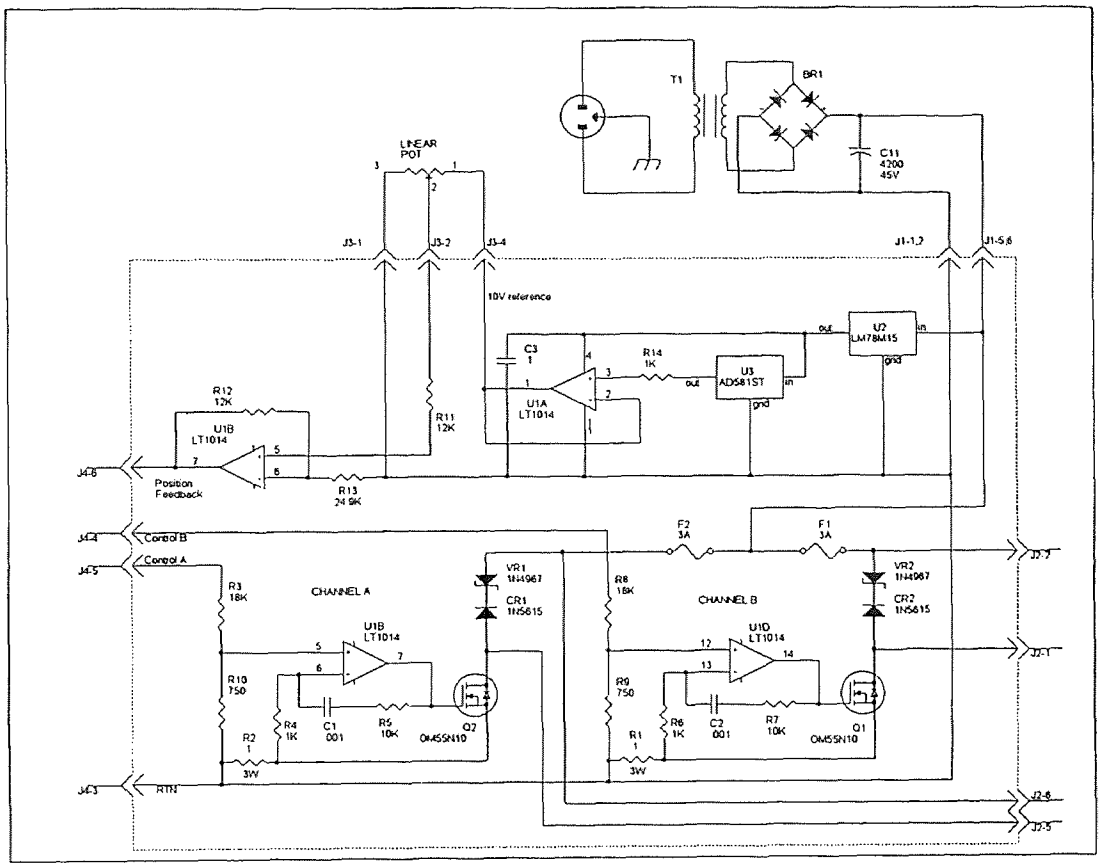

Figure A.1 Schematic Custom Electronics

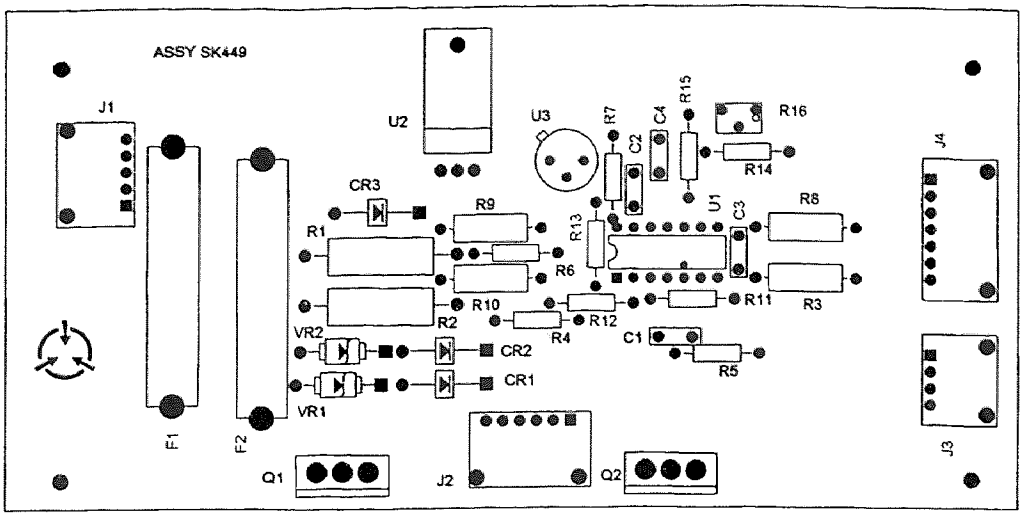

Figure A.2 Custom Electronics PCB Layout

The power supply consists of the power transformer (T1), diode bridge rectifier (BR1), and the filter capacitor (C11). The power supply output is approximately 24VDC and is unregulated.

The 10.00 Volt reference is generated by an Analog Devices Precision Reference I.C. AD584ST. The reference is buffered through the unity gain amplifier (U1A). The buffered output is used as the input to the position feedback potentiometer.

A scaling amplifier is used to maximize useful resolution of the feedback signal by scaling the maximum feedback signal obtained from the potentiometer to full scale of the Analog-to-Digital Converter. The amplifier gain $G = 1 + \frac{R12}{R13}$ is set to provide 0.0 to 10.0 Volt output which corresponds to the extreme right and the extreme left payload positions respectively.

	DESCRIPTION REF DES	PART NO.
BR1	Bridge, Rectifier, 600V, 5A	MDA-2506
C1	Cap, Ceramic, 0.001, μF, 200v	CK05BX102K
C2	Cap, Ceramic, 0.001, μF, 200v	CK05BX102K
C3	Cap, Ceramic, 0.01, μF, 502	CK05BX104K
C11	Cap, Aluminum, 4200 μF, 45V	622D422M05DAA2B
CR1	Diode, Fast Recovery, 1A, 300V	1N5615
CR2	Diode, Fast Recovery, 1A, 300V	1N5615
F1	Fuse, Slow Blow, 3A	MDA-3
F2	Fuse, Slow Blow, 3A	MDA-3
Q1	Mosfet, Power, 55A, 100V	OM55NIO
Q2	Mosfet, Power, 55A, 100V	OM55NIO
R1	Res, Wirewound, 0.1 OHM, 3W	RW69VR10
R2	Res, Wirewound, 0.1 OHM, 3W	RW69VR10
R3	Res, Film, 18K OHM, .1%	RNC60H1802BS
R4	Res, Film, 1K OHM, 2%	RLR07C1001GR
R5	Res, Film, 10K OHM, 2%	RLR07C1002GR
R6	Res, Film, 1K, 2%	RLR07C1001GR
R7	Res, Film, 10K, 2%	RLR07C1002GR
R8	Res, Film, 18K, 0.1%	RNC60H1802KS
R9	Res, Film, 750 OHM, 1%	RNC60H7500FS
R10	Res, Film, 750 OHM, 1%	RNC60H7500FS
R11	Res, Film, 12K, 2%	RLR07C1202GR
R12	Res, Film, 12K, 2%	RLR07C1202GR
R13	Res, Film, 24.9K, 1%	RNC55H2492FS
R14	Res, Film, 1K, 2%	RLR07C1001GR
T1	Transformer, Power	47FJ020
U1	IC, Precision OP-AMP	LT1014J
U2	IC, Voltage Regulator, 15V	LM78M15
U3	IC, Voltage Reference, 10V	AD581ST
VR1	Diode, Zener, 24V, 5W	1N4967
VR2	Diode, Zener, 24V, 5W	1N4967

Table A.1 Parts List Custom Electronics Assembly

Two Voltage Controlled Current Sources were used. The schematic of the Voltage Controlled Current Source is shown in figure A.3. This is a closed-loop pass regulator system. The control voltage scaled by the resistor divider is compared to the voltage induced in the sense resistor by the output current. The resistors R1 and R2 control the steady-state gain *(Iout/Vcontrol)* of the Voltage Controlled Current Source. In this design the resistor ratio was chosen to provide a gain of 0.4 Amperes/Volt. Current limiting is achieved by the virtue of limited control voltage which in this case is 10 Volts. Thus, the maximum current supplied by the Current Source is 4 Amperes.
It should be noted that 4 Ampere current is the intermittent rating for the solenoid current. As a precautionary measure the 3A slow-blow fuses were added in series with power source to each solenoid to avoid solenoid damage due to accidental overload.

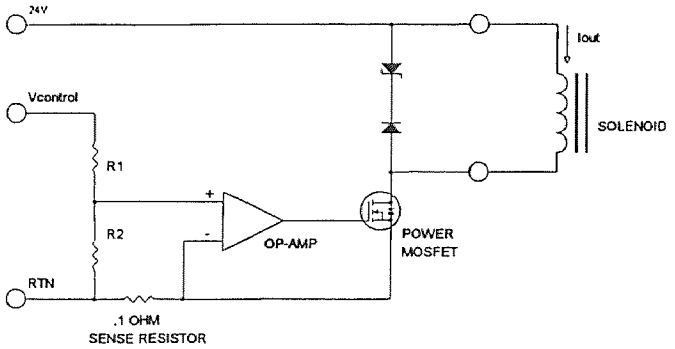

Figure A.3 Schematic Voltage Controlled Current Source

The small-signal operation of the Voltage Controlled Current Source was verified using the Frequency Response System manufactured by NL technologies. Measurements were obtained at 0.2ADC and 1ADC operating points with 20% superimposed variable

frequency signal. The measured results are presented in figures A.4 and A.5 respectivelyThe data were collected using actual solenoid with fully seated plunger as a load.

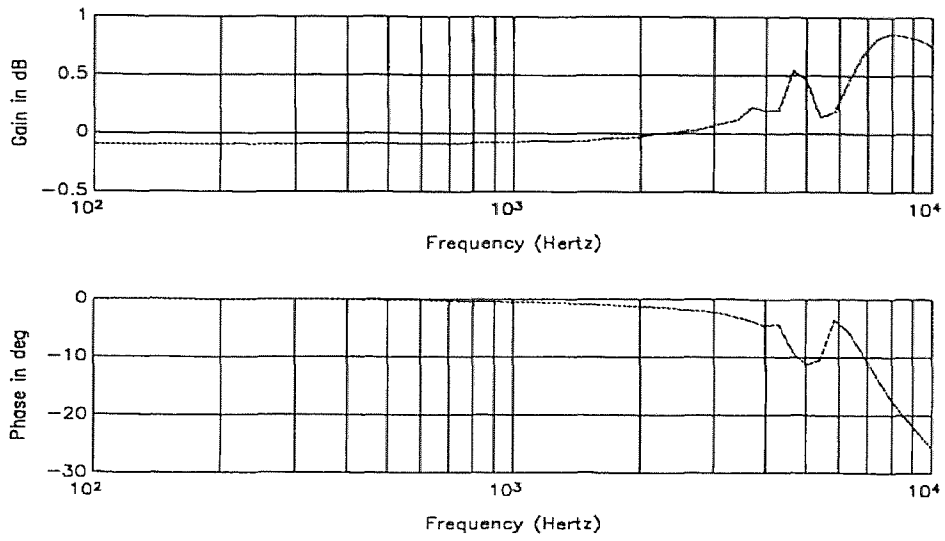

Figure A.4 Frequency response of VCCS Operating point 0.2ADC +0.05AAC

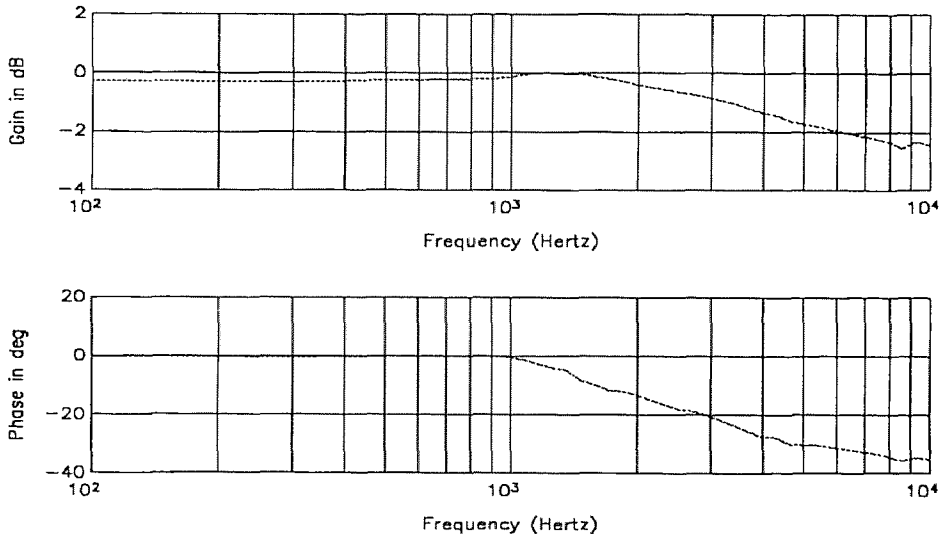

Figure A.4 Frequency response of VCCS Operating point 1ADC +0.2AAC

The large-signal behavior of the Voltage Controller Current Source is dependent on the input supply voltage. The maximum rate of change in the coil current is given by $\frac{dI}{dt} = \frac{V}{L(d)}$ where V is the supply voltage and $L(d)$ is the inductance of the solenoid at a given displacement. This property is demonstrated in figure A.6. With 5 Volt step programming excitation, the output current of the Voltage Controlled Current Source reaches the 2 Ampere level only after 5 milliseconds. The behavior of the Voltage Controlled Current Source under large-signal excitation was approximated in simulation portion of this document with a low-pass filter with 200 Rad/Sec break frequency.

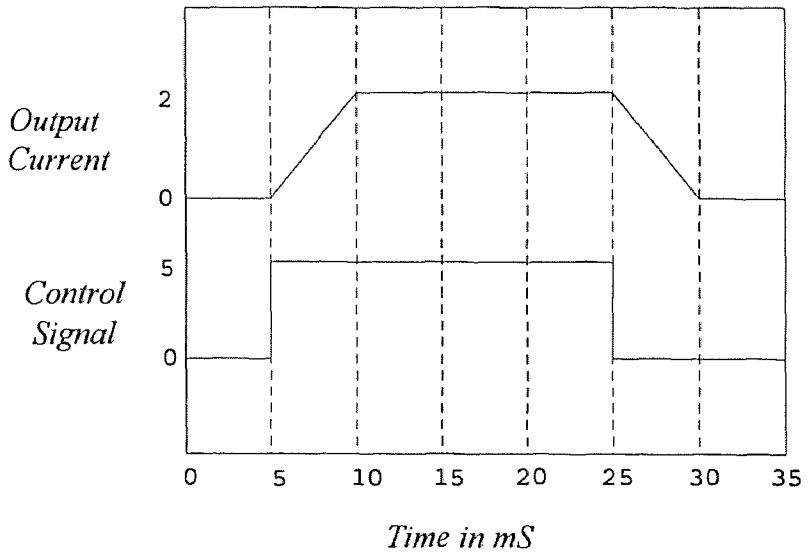

Figure A.6 Voltage Control Current Source Large-Signal Behavior

APPENDIX B

CONTROL PROGRAM SOURCE CODE

This appendix presents the source code listing for the real-time control algorithm used in this research. The code is compatible with Borland Turbo C++ Version 3 compiler.

```
#include <dos.h>
#include <conio.h>
#include <stdio.h>
#include <math.h>
#include "AD2210.h"
#include "AD2210.inc"

#define  Tension          2.0    /* Tension force in Newtons */
#define  MaxCurrent       4.0    /* maximum solenoid current */
#define  AmpScale         0.4    /* Scale of output Amplifier Amps/Volt */
#define  ClockRate     1250.0    /* Number of samples per second */
#define  PotGain       555.2941  /* Volts/meter gain of potentiometer */
#define  PotOffset        0.039  /* Feedback voltage at 0 displacement */
#define  TravelLength     0.017     /* maximum travel distance */
#define  Mass             0.36877   /* Payload mass in Kg */
#define  Friction         1.25      /* Potentiometer actuation force */
#define  RefreshTime      3         /* This program disables all
                                       interrupts for this number of
                                       seconds */
#define  g1             7360.0     /* dLQR gain (distance) */
#define  g2              101.21    /* dLQR gain (velocity) */
#define  k1             0.69881    /* dLQE gain (distance) */
#define  k2              409.25    /* dLQE gain (velocity) */
#define  k3             33175.0    /* dLQE gain (exogen)   */

#define  ArraySize      3750      /* must be larger than
                                     CycleCount*RefreshTime*/

int      toggle = 1;

unsigned int   CycleCount,      /* Auxiliary variable */
               MaxCycle;

float  FbkErr[ArraySize],       /* Position error data storage */
       EstFrs[ArraySize];       /* Estimated Force data storage */

double  Position,           /* Payload position */
      RefPosition,          /* Reference position */
      Force,                /* Calculated control output at time (k) */
      ForceRight,           /* Estimated force in the right solenoid */
      ForceLeft,            /* Estimated force in the left solenoid */
      ExoForce,             /* Estimated Exogenous Force */
      Feedback,             /* feedback storage */
      Error,                /* Positioning Error */
      CurrentRight,         /* Excitation current in right solenoid */
      CurrentLeft,          /* Excitation current in left solenoid */
      PositionError,        /* Positioning Error  */
      PositionRight,        /* displacement wrt right solenoid */
      PositionLeft,         /* displacement wrt left solenoid */
      Position_1,           /* position at last sampling (k-1) */
      Velocity,             /* payload velocity */
      L1,                   /* coefficients to simplify Kalman filter */
      L2,                   /* calculations */
      L3,
      L4,
      L5;
```

```
/*****************

 AToDConversion

 The AToDConversion function samples from the specified channel and
 returns the digitized value.

*****************/

int AToDConversion(unsigned char Channel)
{
 SetChannel(Channel);              /* Set the channel from which to
                                      sample */
 StartConversion();                /* Start a conversion */

 while (ConversionDone() == 0);    /* Wait until data is ready */

 return(ReadData());               /* Return digitized value */
 }

void main(void)
{  /* main */

FILE    *out;


InitializeBoardSettings(768, 10.0, UNIPOLAR);
/* Set base address and volt range*/
  DACSlope = 409.5;       /* 12 bit resolution gain */
  DACOffset = 0.0;        /* no offset for unipolar operation */
  clrscr();
  ResetBoard();
  SetUserClock(ClockRate);
  SetExternalTrigger(DISABLED);       /* Use internal/software trigger */
  SetGain(1);
   gotoxy(12,8);
   cprintf("<<<<<<<   SINGLE-AXIS AGONISTIC MOTION CONTROL   >>>>>>");
   gotoxy(30,24);
   cprintf("Press any key to exit");
   gotoxy(22,12);
   cprintf("Data refreshed every %4i seconds", RefreshTime);

/********************* INITIALIZE VARIABLES ****************************/

   ExoForce=0.0;
   Position_1 = 0.0,
   Velocity = 0.0;

/******************* CALCULATE KALMAN FILTER COEFFICIENTS *************/

  L1=k1 + k2/ClockRate + k3/pow(ClockRate,2)/2/Mass;
  L2=k2 + k3/ClockRate/Mass;
  L3=k3;
  L4=1/pow(ClockRate,2)/2/Mass;
  L5=1/ClockRate/Mass;

/*************************************************************************/
```

```
    while (!kbhit())
    {  /* while !kbhit */

     disable();
     gotoxy(30,14);
     cprintf("Feedback is %0.9f",Feedback);
     gotoxy(30,16);
     cprintf("ExoForce is %0.9f",ExoForce);
     gotoxy(30,18);
     cprintf("PositionError is %0.5e",fabs(PositionError));

     MaxCycle=RefreshTime*ClockRate;


     /******* toggle the reference *******/

     toggle = !toggle;
     RefPosition = TravelLength*(0.8 - 0.6*toggle);

     /************************************/

     Feedback = DigitalToReal(AToDConversion(0));
     Feedback = (Feedback-PotOffset)/PotGain;


     CycleCount = 0;

     while (CycleCount < MaxCycle)
     {  /*while count*/

     while (ClockDone(2) == FALSE); /*Wait until clock done with cycle */


/***************************** GET FEEDBACK *****************************/

   Feedback = DigitalToReal(AToDConversion(0));
   Feedback = (Feedback-PotOffset)/PotGain;


/************************** OBSERVER DYNAMICS **************************/


   Error = (Position_1 - Position);

   Position = Position+Velocity/ClockRate+L4*(Force+ExoForce)+L1*Error;

   Velocity = Velocity+L5*(Force+ExoForce)+L2*Error;

   ExoForce = ExoForce+L3*Error;

   Position_1 = Feedback;


 /********************* CONTROL LAW CALCULATION **********************/

   Force = - g1*(Position-RefPosition) - g2*Velocity - ExoForce;
   /* Control Law u[k]=-G*x[k]-G0x0 */
```

```
 /****************** DETERMINE FORCE DISTRIBUTION *********************/

   if (Force > 0)
      {
       ForceRight = Tension;
       ForceLeft = Force+Tension;
      }
    else
      {
       ForceRight = -Force+Tension;
       ForceLeft = Tension;
      }

/************ CALCULATE CORRESPONDING CURRENT PROGRAMMING SIGNALS ******/

   PositionRight = Feedback + Velocity/ClockRate;

  /* protection against erroneous readings */

  if (PositionRight < 0.0) PositionRight = 0.0;
  if (PositionRight > TravelLength) PositionRight = TravelLength;
  PositionLeft  = TravelLength - PositionRight;
  /* calculate currents */
  CurrentRight=sqrt(fabs((pow(ForceRight,2)+45.699*ForceRight)
  *(47.003*pow(PositionRight,2)+0.4312*PositionRight+0.000204)));
  if (CurrentRight > MaxCurrent)
     {
      CurrentRight = MaxCurrent;            /* Limit output current */
      /* correct for saturation */
      Force = -Tension + 22.835 - sqrt(fabs(521.423+pow(MaxCurrent,2)/
      (47.003*pow(PositionRight,2)+0.4312*PositionRight+0.000204)));
      }
  CurrentLeft=sqrt(fabs((pow(ForceLeft,2)+45.699*ForceLeft)
  *(47.003*pow(PositionLeft,2)+0.4312*PositionLeft+0.000204)));
  if (CurrentLeft > MaxCurrent)
     {
      CurrentLeft = MaxCurrent;
      Force = Tension -22.835 + sqrt(fabs(521.423+pow(MaxCurrent,2)/
      (47.003*pow(PositionLeft,2)+0.4312*PositionLeft+0.000204)));
      }

/************************ OUTPUT THE CONTROL **************************/

UpdateDAC(2,CurrentRight/AmpScale); /* Send current in right solenoid */
UpdateDAC(1,CurrentLeft/AmpScale);  /* Send current in left solenoid */

  PositionError = Position - RefPosition;
  FbkErr[CycleCount] = Feedback - RefPosition;
  EstFrs[CycleCount] = Force;

  CycleCount++;
  while (ClockDone(2) == TRUE);    /* Wait until clock restarts cycle */
  }   /* while count */
 }    /*while kbhit */

 UpdateDAC(1, 0.0);          /* Set Left solenoid current to 0.0 amps */
 UpdateDAC(2, 0.0);          /* Set Right solenoid current to 0.0 amps */
```

```
/************************** DATA RECORDING ***************************/

 clrscr();
 cprintf("Data stored in file Data.out");

 out = fopen("data.out", "w+b");
 for (CycleCount = 0; CycleCount < MaxCycle; CycleCount++)
 {
 fprintf(out,"%e %e \n", FbkErr[CycleCount], EstFrs[CycleCount]);
 }
 fclose(out);

/*********************************************************************/

}   /*main */
```

BIBLIOGRAPHY

[1] Friedland, Bernard. *Control System Design: An Introduction to State Space Methods.* New York: McGraw-Hill, 1986.

[2] Friedland, Bernard. *Advanced Control System Design.* In Preparation

[3] Lewis, Frank L. *Applied Optimal Control & Estimation: Digital Design & Implementation* Englewood Cliffs: Prentice Hall 1992

[4] Hsu, Jay C. & Meyer, Andrew,U. *Modern Control Principles and Applications.* New York: McGraw-Hill 1956

[5] Chen, Jian *Computer control for 2-Axis Magnetic Suspension System,* Masters Thesis New Jersey Institute of Technology January 1991.

[6] Plonus, Martin, A. *Applied Electromagnetics.* New York: McGraw-Hill, 1978.

[7] Zahn, Marcus. *Electromagnetic Field Theory: A Problem Solving Approach* . New York: John Wiley & Sons, 1979

[8] Haessig, David. *Selection of LQR/LTR Design Coefficients Trough Constrained Optimization,* Proceedings IEEE Regional NY/NJ Control Conference, 1994.